Structural assessment using terrestrial laser scanning point clouds

Linh Truong-Hong
Delft University of Technology, Delft, The Netherlands

Roderik Lindenbergh
Geoscience and Remote Sensing, Delft University of Technology, Delft, The Netherlands, and

Thu Anh Nguyen
Faculty of Civil Engineering, Ho Chi Minh City University of Technology, Ho Chi Minh City, Vietnam and Vietnam National University Ho Chi Minh City, Ho Chi Minh City, Vietnam

Abstract

Purpose – Terrestrial laser scanning (TLS) point clouds have been widely used in deformation measurement for structures. However, reliability and accuracy of resulting deformation estimation strongly depends on quality of each step of a workflow, which are not fully addressed. This study aims to give insight error of these steps, and results of the study would be guidelines for a practical community to either develop a new workflow or refine an existing one of deformation estimation based on TLS point clouds. Thus, the main contributions of the paper are investigating point cloud registration error affecting resulting deformation estimation, identifying an appropriate segmentation method used to extract data points of a deformed surface, investigating a methodology to determine an un-deformed or a reference surface for estimating deformation, and proposing a methodology to minimize the impact of outlier, noisy data and/or mixed pixels on deformation estimation.

Design/methodology/approach – In practice, the quality of data point clouds and of surface extraction strongly impacts on resulting deformation estimation based on laser scanning point clouds, which can cause an incorrect decision on the state of the structure if uncertainty is available. In an effort to have more comprehensive insight into those impacts, this study addresses four issues: data errors due to data registration from multiple scanning stations (*Issue 1*), methods used to extract point clouds of structure surfaces (*Issue 2*), selection of the reference surface S_{ref} to measure deformation (*Issue 3*), and available outlier and/or mixed pixels (*Issue 4*). This investigation demonstrates through estimating deformation of the bridge abutment, building and an oil storage tank.

Findings – The study shows that both random sample consensus (RANSAC) and region growing–based methods [a cell-based/voxel-based region growing (CRG/VRG)] can be extracted data points of surfaces, but RANSAC is only applicable for a primary primitive surface (e.g. a plane in this study) subjected to a small deformation (case study 2 and 3) and cannot eliminate mixed pixels. On another hand, CRG and VRG impose a suitable method applied for deformed, free-form surfaces. In addition, in practice, a reference surface of a structure is mostly not available. The use of a fitting plane based on a point cloud of a current surface would cause unrealistic and inaccurate deformation because outlier data points and data points of damaged areas affect an accuracy of the fitting plane. This study would recommend the use of a reference surface determined

based on a design concept/specification. A smoothing method with a spatial interval can be effectively minimize, negative impact of outlier, noisy data and/or mixed pixels on deformation estimation.

Research limitations/implications – Due to difficulty in logistics, an independent measurement cannot be established to assess the deformation accuracy based on TLS data point cloud in the case studies of this research. However, common laser scanners using the time-of-flight or phase-shift principle provide point clouds with accuracy in the order of 1–6 mm, while the point clouds of triangulation scanners have sub-millimetre accuracy.

Practical implications – This study aims to give insight error of these steps, and the results of the study would be guidelines for a practical community to either develop a new workflow or refine an existing one of deformation estimation based on TLS point clouds.

Social implications – The results of this study would provide guidelines for a practical community to either develop a new workflow or refine an existing one of deformation estimation based on TLS point clouds. A low-cost method can be applied for deformation analysis of the structure.

Originality/value – Although a large amount of the studies used laser scanning to measure structure deformation in the last two decades, the methods mainly applied were to measure change between two states (or epochs) of the structure surface and focused on quantifying deformation-based TLS point clouds. Those studies proved that a laser scanner could be an alternative unit to acquire spatial information for deformation monitoring. However, there are still challenges in establishing an appropriate procedure to collect a high quality of point clouds and develop methods to interpret the point clouds to obtain reliable and accurate deformation, when uncertainty, including data quality and reference information, is available. Therefore, this study demonstrates the impact of data quality in a term of point cloud registration error, selected methods for extracting point clouds of surfaces, identifying reference information, and available outlier, noisy data and/or mixed pixels on deformation estimation.

Keywords Laser scanning, Point cloud, Structural assessment, Surface damage, Deformation, RANSAC, Region growing

Paper type Research paper

1. Introduction

Laser scanning, also known as light detection and ranging (LiDAR), has been used to quickly and accurately acquire three-dimensional (3D) topographic data of visible surfaces. The fundamental principle of LiDAR involves a laser beam to measure the distance from the instrument to a surface of an object based on the time of travel between signal transmission and reception called a laser pulse, and a 3D coordinate of an intersection point between the laser pulse and the surface is computed. The output datasets consisting of x-, y-, z-coordinates associated with other attributes are commonly referred to as a 3D point cloud. One of the LiDAR units is a terrestrial laser scanner (TLS), the laser sensor operating from the ground capturing great details of surfaces of objects with millimetre accuracy. Thus, this type of laser scanning data has been used in civil engineering like construction progress monitoring, and dimensional quality control (Son and Kim, 2010), construction management (Bosché, 2010), road modelling (Boyko and Funkhouser, 2011; Truong-Hong *et al.*, 2019) and disaster planning (Laefer and Pradhan, 2006). Interestingly, it is also being applied for structural assessment, for example, creating geometric models for Finite element (FE) mesh generation (Truong-Hong *et al.*, 2012; Kassotakis *et al.*, 2020), determining surface damage (Mizoguchi *et al.*, 2013; Sedek and Serwa, 2016) and deformation measurement (Bosché and Guenet, 2014; Truong-Hong and Lindenbergh, 2019). The deformation measurement has attracted both academia and professional communities because laser scanning can give high accuracy of deformation of an entire surface of a structure instead of discrete locations on the surface obtained from traditional survey methods.

In structural assessment–based deformation analysis, both relative and absolution deformation estimation are required to assess behaviour of individual members and an entire structure. Particularly, for large-scale structures, including dams, tunnels and bridges, the absolution deformation may give information on the interaction between the structure and the surrounding environment. For example, the absolution deformation of a dam may be related to the water level of a reservoir (Yigit *et al.*, 2016), or a tunnel movement may result in ground settlements–induced building damage (Giardina *et al.*, 2019). To estimate relative

deformation, geometric data of the structure in the same local coordinate system can be used (Lindenbergh and Pietrzyk, 2015; Jiang *et al.*, 2021), while a geodetic network is required to record deformation/movement of the structure when estimating absolute deformation (Kavvadas, 2005). When laser scanning is used to estimate the absolute deformation, a point cloud of a single scan station is registered into the geodetic coordinate system, which may result in increasing the total error budget (Lichti Derek *et al.*, 2005). Moreover, for large-scale structures, laser scanning often captures the structure at low temporal frequency (e.g. monthly or yearly) because of budget limitations. Alternative methods, for example global navigation satellite system (GNSS) (Montillet *et al.*, 2016; Xi *et al.*, 2021), are often installed on a structure to record movement at specific locations with high frequency at lower costs. However, these methods measure at only fixed locations of the structure and local behaviour of the structure can be missed (Harmening and Neuner, 2020). This paper presents the use of a laser scanner to estimate deformation of small-scale structures, and particularly focuses on relative deformation, such that georeferencing of the point cloud is excluded.

A typical workflow for deformation analysis consists of four main steps: data acquisition, data registration, point cloud extraction and deformation estimation. Several studies have proposed and discussed solutions for each individual step. For example, first, in identifying the influence of scanning parameters on data quality, Soudarissanane *et al.* (2011) and Laefer *et al.* (2009) remarked that the precision of a point cloud decreases when the incidence angle and scanning measurement increases, particularly for incidence angles larger than 70 degrees. Second, Cheng *et al.* (2018) gave a brief overview of data registration methods and reported that the point cloud registration error depends on the quality of data points, and can vary between 3 mm and 22 m. Third, in discussing segmentation methods, Xie *et al.* (2020) addressed that the accuracy of the segmentation relies on various parameters, for example, region growing depends on the growing criteria and selected seeding points. Finally, in a survey of the use of TLS point clouds for structural deformation measurement, Truong-Hong and Laefer (2014) noted that errors of deformation estimation–based point clouds varied from 9 mm to 30 mm. These studies discussed advantages and disadvantages of methods for specific applications, for example, monitoring structural deformation or measuring vertical clearance of a bridge. Considering various effects of the methods used in a complete workflow for deformation measurements based on TLS point clouds has not been addressed, the main contributions of the paper are as follows:

(1) investigating point cloud registration error affecting resulting deformation estimation;

(2) identifying an appropriate segmentation method used to extract data points of a deformed surface;

(3) investigating a methodology to determine an un-deformed or a reference surface for estimating deformation;

(4) proposing a methodology to minimize the impact of outlier, noisy data and/or mixed pixels on deformation estimation.

Finally, a bridge abutment, building and steel frame of a storage oil tank were selected as case studies to demonstrate this study.

2. Related work
For the last two decades, laser scanning has been widely used to acquire topographic and texturing information of surfaces of structures for inspection and assessment. To date, most studies use laser scanning point clouds to identify surface deficiencies (e.g. water leakage or

moisture), determine material loss (area and volume losses) and deformation measurement, which are investigated in this section, while other applications of the point cloud can refer to Laefer (2020).

For detecting surface damage appearing through texturing information, for example, water bleeding, chemical attack and corrosion/crusting, intensity and/or colour of a point cloud were used. For example, Armesto-González et al. (2010) used machine learning–based intensity images of 3D point cloud to detect moisture of surfaces, in which the point clouds acquired from various scanners (e.g. FARO Photon, TRIMBLE GX200, and RIEGL-Z390i) were used to investigate influence of intensity variance on resulting detection. Similarly, Suchocki et al. (2020) proposed segmentation-based intensity values of a point cloud to extract an area subjected to moisture and biofilm. Interestingly, the authors reported that damage detection based on the point cloud from the phase shift scanner is more sensitive than that from the time-of-flight scanner. Additionally, Tan et al. (2016) found a linear model between the point cloud and water content intensity when detecting water leakage of a tunnel.

For example, to estimate volume loss of a reinforced concrete beam column, Olsen et al. (2010) proposed the crossing section method to determine a polygon fitting a perimeter of a cross-section, and the volume loss was computed from the polygon areas and interval distances between adjacent cross-sections. Teza et al. (2009) detected damage area by analysing Gaussian curvature of sub-area of a region of interest, but missed detection can occur if the noise of the point cloud exceeded 8 mm. Similarly, distance and gradient computed from rectangular grids of a selected area to a reference plane were used to detect defective areas of the pile cap, in which a predefined distance and gradient thresholds were used to classify damaged and undamaged grids (Liu et al., 2011). Suchocki and Błaszczak-Bąk (2019) defined that data points of crack face and the cavity of brick walls have distances to a reference surface more than 5 mm, in which the reference surface was determined from entire points of the wall. Additionally, to measure the surface loss of a steel beam due to corrosion, Truong-Hong and Laefer (2015b) used an angle criterion based on a 2D grid to extract point clouds on a boundary of a hole, and an area of the hole was then computed from a polygon fitting through the boundary points.

In addition, in attempting to use laser scanning to measure crack on a surface of a structure, Truong-Hong et al. (2016) mapped Red-Green-Blue (RGB) images on a point cloud of a masonry abutment to assist users in identifying locations of cracks. Next, Cabaleiro et al. (2017) used an alpha shape method to extract data points on a boundary of crack of a timber beam and reported that the method can extract the crack width more than 3 mm for a sampling step of 1 mm. For documenting the cracks on substructures of a bridge, Valença et al. (2017) map cracks detected from the 2D image onto a point cloud, in which the crack face is known as discontinuity of the surface is determined from the point cloud. However, as noise and spatial information of data points, crack extraction based on the laser scanning point cloud can obtain the best performance if the crack width is more significant than 5 mm.

This study aims to investigate factors that affect resulting deformation estimation. The rest of this section is restricted to investigating recent works relating to deformation measurement based on TLS point clouds. Many methods have been proposed to analyse a point cloud for change detection or deformation measurement. For example, a cloud-to-cloud method measured deformation through a distance from any point of the reference surface to its nearest neighbour point in the sampling surface (Girardeau-Montaut et al., 2005). Additionally, Lague et al. (2013) proposed a multiscale model to model cloud comparison for change detection through an average distance between two sub-clouds from the reference and sampling surfaces, in which the cylinder neighbourhood is used to extract the sub-cloud. Those methods are mainly used for topographic change detection. Following this, the work of using point clouds for measuring deformation of the civil engineering structure is surveyed.

Bosché and Guenet (2014) inspected the flatness of the building floor by mapping a 3D point cloud to an as-design building information modelling (BIM) model to measure the

deviation between the point cloud and BIM by using a straightedge and F-numbers methods. Tang *et al.* (2011) proposed three algorithms consisting of range filtering, deviation filtering and sliding window to inspect floor defects through deviations between the points and the reference surface. The main difference between these methods is the different methodologies used to denoise the point clouds of the surfaces. Li *et al.* (2020) determined the flatness of a concrete surface by distances between the points of the surface to the reference surface estimated from 80% points of the surface, in which random sample consensus (RANSAC) was carried out (Schnabel *et al.*, 2007).

In measuring deformations of a heritage structure, Bertacchini *et al.* (2010) used a centroid of each horizontal slice along a vertical direction of the tower to determine deviation from verticality (out-of-plumb) of the Asinelli Tower in Bologna, in which the interval thickness of the slice was 10 cm. Pesci *et al.* (2013) investigated the effects of noisy data and selected reference information in evaluating building deformation due to seismic activity by using TLS point clouds. The buildings were scanned from various scanning ranges and angles, while point-to-primitives (e.g. planes or cylinders) were computed to determine building deformation. The study recommended that the high incidence angle must be quantified before using point clouds for measuring deformation, and the primitive shape strongly depends on the spatial distribution of the point cloud. Moreover, based on knowing the shape of a tower of the Ayutthaya temples, Thailand, the cylinder fitting was used to reconstruct the tower from its point cloud, and the axis along a longitudinal direction of the cylinder is used to measure a tilt angle of the tower (Bhadrakom and Chaiyasarn, 2016).

To measure the deformation of an individual girder of a bridge, Lichti *et al.* (2002) compared fitting lines of the top and bottom wood stringers of the bridge under unloaded and loaded conditions to determine vertical displacements. Moreover, Paffenholz *et al.* (2008) subdivided a point cloud of the girder surface into 2D cell-grids with cell size of 0.25 m and used the median of z coordinates of each cell to determine vertical displacements of the bridge in a static loading test. Zogg and Ingensand (2008) monitored deformations of the Felsenau Bridge subjected to a static load of 54 tons performed at several viaduct sections. Third-party software was used to determine vertical displacements by comparing the 3D point cloud from the unloaded condition against the loaded condition. The TLS-based results were no more than 3.5 mm larger than ones based on precision levelling. Moreover, in measuring a vertical clearance of bridges, Riveiro *et al.* (2013) fitted a point cloud of a beam camber and pavement by a polynomial curve and a plane, respectively, while the vertical clearance was the difference of z values computed from the curve and the plane. Truong-Hong and Lindenbergh (2019) proposed point–surface, point–cell and cell–cell methods, in which the high order polynomial surfaces or multiple planar patches were used to describe the bottom surfaces of the girders, while the vertical clearance is defined as distances from the points describing a road surface to the bottom surfaces of the girders.

On another application, Van Gosliga *et al.* (2006) measured the deformation of a bored tunnel by comparing the point cloud to a fitting cylinder model of the tunnel derived from a sub-data set. To measure displacements of a load-test beam, similar to a cell-to-cell method proposed by Truong-Hong and Lindenbergh (2019), Cabaleiro *et al.* (2020) divided a bottom surface into rectangular meshes, and deformations are distances between the centroid of the element mesh from different load stages, in which the centroid of the element is computed, and the data points within the mesh. The authors addressed that an error of the deformation measurement is less than ±0.02 mm when a high precision scanner with the accuracy of ±0.025 mm is used in acquiring the point cloud.

In summary, although a large amount of the studies used laser scanning to measure structure deformation in the last two decades (Mukupa *et al.*, 2017), methods mainly applied to measure change between two states (or epochs) of the structure surface and focus on quantifying deformations-based TLS point clouds. Those studies proved that a laser scanner

could be an alternative unit to acquire spatial information for deformation monitoring. However, there are still challenges in establishing an appropriate procedure to collect a high quality of point clouds and developing methods to interpret the point clouds to obtain reliable and accurate deformation, when uncertainty, including data quality and reference information, is available. Therefore, this study demonstrates the impact of data quality in a term of point cloud registration error, selected methods for extracting point clouds of surfaces, identifying reference information, and available outlier, noisy data and/or mixed pixels on deformation estimation.

3. Structural assessment-based deformation
After data acquisition and preprocessing, a deformation estimation–based point clouds procedure consists of two main steps: (1) extracting a point cloud of a surface of a structural component, (2) estimating the deformation. The first step is executed through point cloud segmentation methods, for example, region growing (Rabbani *et al.*, 2006), Hough transforms (Hough, 1959), and RANSAC (Schnabel *et al.*, 2007). However, due to complexity, difficulty in implementation and selecting parameters, the region growing and RANSAC are primarily selected to implement and use in practice (Cloudcompare, 2021; Leica Geosystems, 2020). As such, region growing-based methods (Vo *et al.*, 2015; Truong-Hong and Lindenbergh, 2020) and RANSAC (Schnabel *et al.*, 2007) implemented (Cloudcompare, 2021) are used to extract data points of surfaces of a structure to investigate an impact of segmentation methods on accuracy of deformation estimation.

3.1 Region-growing based segmentation method
Region growing–based methods are an iterative process to extract points having deviations of salient features (e.g. orthogonal distances and normal vectors) satisfying predefined criteria, and these points are recognized as the same segment. A popular region growing segmentation is the work of Rabbani *et al.* (2006), who used two salient features (a normal vector and residual) of data points as criteria for a growing process. In this implementation, for each point, the normal vector is normal of a plane fitted through neighbouring points, and the residual is the root mean square distances from the neighbour points to the fitting plane, in which the neighbouring points can be extracted either k-nearest neighbour (kNN) or radius neighbour search. The growing process starts with the point having the smallest residual as an initial seeding point, and its neighbour points are known as the same region with the seeding point if deviations of their normal vectors satisfy a predefined angle threshold. Any adding points having a residual less than a predefined residual threshold is considered as the seeding point in the next iteration. The process iteratively extracts the points for the region until no points are added to the region, and is completed when all points are examined.

However, region growing segmentation is required to determine salient features for each point, and the region growing process must check every point, which imposes intensive computation (Vo *et al.*, 2015). As such, in this study, to avoid intensive computation, cell-based and voxel-based region growing methods(CRG and VRG) (Vo *et al.*, 2015; Truong-Hong and Lindenbergh, 2020), which are basically similar to the region growing segmentation proposed by Rabbani *et al.* (2006), are implemented, in which the region growing process is based on local planes within cells for CRG or voxels for VRG. A point cloud was first decomposed into small cells/voxels in these methods, and points within each cell/voxel were subsequently used to extract local planes. Next, the local planes associated with salient features (e.g. a normal vector and residual) were used as input data in CRG and VRG to recognize points of surfaces. As the local planes within the cells or voxels were used, an additional condition known as the deviation of distances between local planes was included in determining if the patches or

voxels were to be added to the same region of a seeding cell/voxel. Differing from point-based region growing developed by Rabbani *et al.* (2006), both CRG and VRG are required additional steps known as boundary refinement. That is because either cells or voxels on a boundary of a region may contain data points of adjacent regions. The step is done based on distances from the points within the boundary cells or voxels to adjoined regions. For more details of CRG and VRG, one can refer to (Vo *et al.*, 2015; Truong-Hong and Lindenbergh, 2020). Additionally, required input parameters of CRG and VRG are cell/voxel size (c_{s0} *or* v_{s0}), angle (α_0) and distance (d_0) and residual (res_0) thresholds.

3.2 Random sample consensus

A RANSAC method iteratively extracts a random sub-data set to construct a surface of a shape primitive. A resulting surface is evaluated by a score function established from the best-fitted points (or inlier points) of the shape candidate. The inlier points are determined as the points having Euclidean distances to the shape primitive less than a predefined buffer or distance threshold. Following the number of trails, the best shape primitive is the model having the highest score. Additionally, the remaining data set is subsequently used to extract the data points of other shape primitives. In this paper, the RANSAC method developed by Schnabel *et al.* (2007) and implemented in CloudCompare opensource (Cloudcompare, 2021), which is widely accessed and used by both professional and academic communities, is selected to extract the point cloud of surfaces of the structure. The method was developed based on the RANSAC paradigm with several refinement steps as follows:

Input data are a set of data point cloud $P = \{p_i = (x_i, y_i, z_i) \in R^3, i = [1, N]\}$ and a normal vector $n_i = \{nx_i, ny_i, nz_i\}$ of each point. The algorithm randomly selects a minimum sub-data set to establish a shape primitive. For example, it requires three points to detect a plane. In addition, a function score, $\sigma_P(\psi) = |P_\psi|$, based on the number of points P_ψ is used to evaluate the candidate primitive shape (ψ). The points P_ψ are determined in two consecutive steps: (1) determining the compatible points (P'_ψ) of the candidate shape primitive ψ and (2) using a connected component analysis to eliminate spurious surfaces due to parallel surfaces of the shape available in a data set. In the former step, the compatible points (P'_ψ) are determined through two parameters including ε, the maximum distance of the points to the primitive shape ψ, and α, the deviation angle between the normal vector of the point (p_i) and the normal vector of the shape (Equation 1). Notably, this implementation requires searching the number of the compatible points P'_ψ larger than a predefined minimum number (*min_ptc*) to determine the candidate shape primitive (Schnabel *et al.*, 2007).

$$P'_\psi = (p|p\varepsilon P) \text{ if } d(p, \psi) \leq \varepsilon \text{ and } \angle n(p)n(\psi, p) \leq \alpha \tag{1}$$

where $d(p, \psi)$ denotes the Euclidean distance from the point $p \in P$ to the primitive shape ψ, $n(p)$ is the normal vector of the point p, and $n(\psi, p)$ is the normal vector of the shape at the location that the point p is projected onto the shape ψ.

In the latter step, the data points P'_ψ are then projected onto the primitive shape ψ to create a bitmap with a predefined sampling resolution or pixel size (β). Next, a connected component is applied to the bitmap image to determine the largest component, and the data points corresponding to this component are known as the point P_ψ of the shape primitive.

Finally, when the best candidate shape primitive is identified, a least square method is employed to fit a geometric shape of the shape, and the compatible points having distances to the fitted shape less than 3ε are considered as the final points of the shape primitive. For more details of RANSAC implemented into Cloudcompare (2021), one can refer to the work of Schnabel *et al.* (2007). In summary, to detect the shape primitive from a point cloud, the RANSAC method (Schnabel *et al.*, 2007) requires defining four parameters: (1) the minimum number of points (*no_ptc*$_{min}$) required to identify the candidate shape primitive, (2) the

maximum distances (ε_{max}) between the points and the primitive shape, (3) the maximum deviation angle (α_{max}) between normal vectors of the points and the shape, and (4) the sampling resolution (β).

3.3 Deformation measurement

Once a point cloud of a surface of structure is extracted based on segmentation methods, for example, region growing-based methods and RANSAC mentioned above; the surface deformation is then calculated. The process consists of (1) identifying a reference surface (S_{ref}) and (2) computing deformation as a distance between the reference surface (S_{ref}) and a current surface (S_{sample}). The reference surface can be the structure surface when the structure starts to operate (at time t_0) or after the operation (at time t_i). For the former case, documentation of the surface is mostly not available. In this case, either the surface can be obtained either from as-design documentation or based on contextual knowledge of the structure. For example, the column is perfectly vertical, or two endpoints of the concrete beam are fixed. For the latter case, the structure surface is known or can be acquired by a terrestrial laser scanner, which is similar to the sampling surface S_{sample} (the structure surface at time t_j). In this study, point-to-surface is used to measure distances from the points on the sampling surface S_{sample} to the reference surface S_{ref}. The distances are herein either directional or orthogonal distances, which depends on the purpose of the applications. For example, when measuring a vertical clearance of the bridge, Truong-Hong and Lindenbergh (2019) used the directional distance in the vertical direction. Finally, the deformation herein is a relative deformation of the structure between two states (at time t_0 or t_i vs t_j). Details of the deformation measurement and impact of data and selecting information on resulted measurement are presented through three case studies in the following section. Notably, due to difficulty in a logistic, an independent measurement cannot be established to assess the deformation accuracy based on TLS data point cloud. Notably, due to difficulty in logistics, an independent measurement cannot be established to assess the deformation accuracy based on TLS data point cloud in the case studies of this research. However, common laser scanners using the time-of-flight or phase shift principle provide point clouds with an accuracy in the order of 1–6 mm (Boardman and Bryan, 2018), while the point clouds of triangulation scanners have sub-millimetre accuracy (Haddad, 2011). In practice, the triangulation scanners are rarely used because of their limitations in scanning speed and range measurement.

4. Test bed structures

In practice, the quality of data point clouds and surface extraction strongly impact resulted deformation estimation derived from laser scanning point clouds, which can cause an adverse decision when using such results for structural assessment. To have more comprehensive insight into those impacts, this study addresses four issues: data errors due to data registration from multiple scanning stations (*Issue 1*), methods used to extract point clouds of structure surfaces (*Issue 2*), selection of the reference surface S_{ref} to measure deformation (*Issue 3*), and available outlier, noisy data and/or mixed pixels (*Issue 4*). In *Issue 1*, the impact of the data quality due to registration is demonstrated by comparing deformations derived from a single scanning and multiple scanning stations. Moreover, in *Issue 2*, two popular point cloud segmentation methods, region growing (Vo *et al.*, 2015) and RANSAC (Schnabel *et al.*, 2007) to assess the ability of these methods for segmenting the surface point cloud, which is measured through quantitative evaluations (e.g. F1-score) (Truong-Hong and Laefer, 2015a) by comparing to ground truth (GT). Finally, in *Issue 3*, either contextual knowledge and design documentation or the fitting surface–based point clouds are used as the reference surface S_{ref} for computing deformation of the structure. Investigating this issue would

provide a valuable guideline for practitioners in selecting the appropriate reference surface when it is not explicitly available. Moreover, a moving smooth method based on a spatial interval is introduced to the minimum impact of *Issue 4*. In the following sections, three case studies are used to demonstrate this investigation.

4.1 Lateral deformation of a masonry abutment

An abutment of a metal railway bridge in the Pegnitz Valley, Bayreuth district of Bavaria, Germany, is selected, which was made from block stones. The bridge built in the 1920s has a span of about 37 m. However, after nearly 100 years' service, the abutment was subjected to movements, which can affect the safety of the bridge. As such, the deformation of the abutment components must be estimated to establish maintenance planning. A Leica P20 scanner with a scanning range from 0.4 m to 120 m, point accuracy of 3 and 6 mm for a range measurement of 50 and 100 m, and angular accuracy of 0.002 degree was used to collect point clouds of the abutment (Leica Geosystems, 2021). The scanner was set up about 8 m from the abutment, which allows capturing front and side surfaces of the abutment from a single scan station with a sampling step of 6.3 mm at 10 m (Figure 1a). Subsequently, irrelevant points (e.g. points of plants and a superstructure) were manually removed from the Leica Cyclone (Leica Geosystems, 2020), and the remaining point cloud was down-sampled with the sampling step by 10 mm before exporting their x-, y- and z-coordinates for deformation estimation (Figure 1b).

As the abutment was scanned from a single location, a registration procedure is not required during pre-processing, which implies that there is no registration error. This case study focuses on investigating *Issue 2* and *3*. For *Issue 2*, RANSAC (Schnabel *et al.*, 2007) implemented in Cloudcompare (2021) and VRG (Vo *et al.*, 2015) to extract point clouds of abutment components were used. For RANSAC, input parameters are $no\_ptc_{min} = 100,000$ points, $\varepsilon_{max} = 10$ mm, $\alpha_{max} = 5.0$ degrees, and $\beta = 0.25$. However, before extracting point clouds of surface, a normal vector of each point is estimated, which is normal of a plan fitted through its neighbouring points. In this study, a range search with a searching radius of 0.1 m is used to retrieve the neighbouring points for each given point. Moreover, for VRG, input parameters are empirically selected as follows: $vs_0 = 0.25$ m, $\alpha_0 = 5.0$ degrees, $d_0 = 10$ mm and $res_0 = 10$ mm. *Issue 2* is to investigate an appropriate segmentation method to extract the structure surfaces, and it is unnecessary to select the same input parameters for both methods. However, in this case study, they were selected nearly the same, for example, pairs of parameters, ε_{max} and d_v, and α_{max} and α_v, respectively, describe deviation of distances and normal between the points and the model, while and a pair of β and vs_0 is examined if the points can be considered to check if they are part of the model.

Results of the segmentation derived from RANSAC and VRG based on input point clouds in Figure 1b are shown in Figure 2. Both methods extract the points of the abutment components properly. However, RANSAC extracts the wing wall as two segments (Figure 2a), which implies that the wing wall is subjected to large deformation, and the primitive plane is not suitable to represent an entire wing wall. Moreover, the resulting segmentation based on RANSAC also excludes points around edges where two components (e.g. wing and ballast walls, and wing and breast walls) are intersected. That is because the normal vectors of those points are significantly different from a normal of the model (Figure 2b). This phenomenon does not occur in resulting segmentations derived from VRG because this method includes a filtering step to refine under- or over-segmentation around edges (Vo *et al.*, 2015).

Resulting surface extraction shown in Figure 2 is evaluated by comparing them to GT manually extracted from the abutment (Figure 1b). A point-based evaluation strategy based on quantitative indicators including a true positive (TP), false positive (FP) and false negative (FN) were used to identify a difference between data points of the abutment components extracted from RANSAC and VRG and those of GT. Evaluation quantities are interpreted through
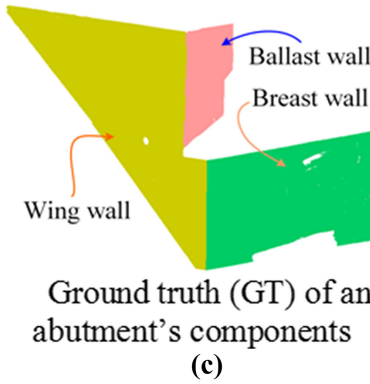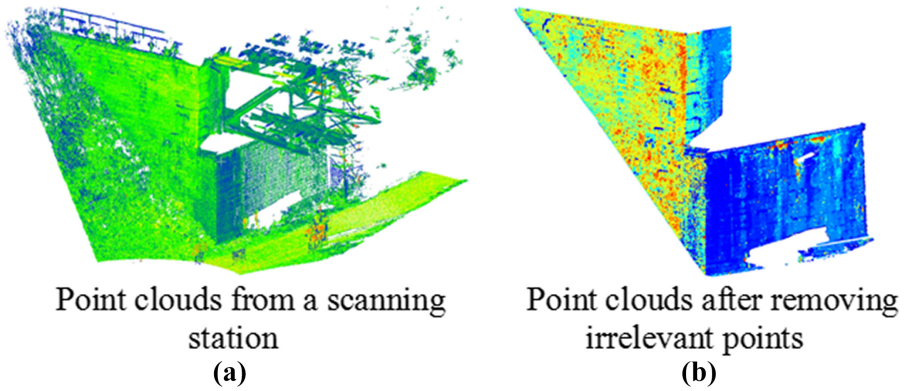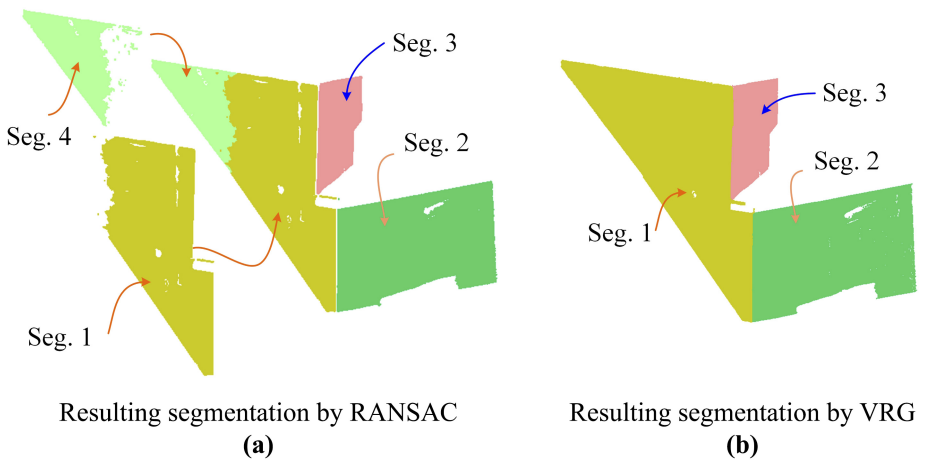
Point clouds from a scanning
station
(a)

Point clouds after removing
irrelevant points
(b)

Ballast wall

Breast wall

Wing wall

Ground truth (GT) of an
abutment's components
(c)

Figure 1.
Point clouds of an
abutment

Seg. 4

Seg. 3

Seg. 2

Seg. 1

Seg. 3

Seg. 2

Seg. 1

Figure 2.
Point clouds of the
abutment components
from RANSAC
and VRG

Resulting segmentation by RANSAC
(a)

Resulting segmentation by VRG
(b)

completeness (*Comp.*), correctness (*Corr.*), and *F1-score*. For a definition of these quantities and the methodology to compute them, one can refer to Truong-Hong and Laefer (2015a).

The evaluation showed that both methods extracted the point clouds of the abutment components with high accuracy. Indeed, Comp., Corr., and *F*1-score were respectively no smaller than 94.3%, 96.6% and 0.969 for RANSAC, and 97.9%, 97.9% and 0.979 for VRG (see Table 1). Generally, VRG extracts the data point of surfaces of the abutment components better than RANSAC. For example, for the wing wall, *F*1-score from VRG is 0.049, larger than that from RANSAC.

For *Issue 3* investigating the impact of a reference surface S_{ref} on deformation estimation, two types of the reference surface S_{ref} are used in this case study. First, the best fitting plane of the abutment components based on their point clouds is considered as the reference surface $S_{ref,fit}$, while second as-design surfaces of the abutment components are assumed as the reference surface $S_{ref,design}$. For the first case, a plane is fitted through the GT point clouds (Figure 1c) of the abutment components by using robust principal component analysis (rPCA) (Laefer and Truong-Hong, 2017) based on a weight covariance matrix cov_w (Equation 2). The fitting plane ($S_{fit} = (p_0, n)$) is defined by a point $p_0 = (x_0, y_0, z_0)$ (Equation 3) and a normal vector $n = (n_x, n_y, n_z)$, which is an eigenvector corresponding to the smallest eigenvalue. The process is iteratively to update the weight of each point to estimate the plane until the difference of fitting residual of two consecutive iterations is no larger than a predefined threshold, $\Delta res_0 = 0.001$, which is empirically selected (Equation 5).

$$\text{cov}_w = \frac{\sum_{p_i \in P} w(p_i)(p_i - p_0)(p_i - p_0)^T}{\sum_{p_i \in P} w(p_i)} \tag{2}$$

$$p_0 = \frac{\sum_{p_i \in P} w(p_i)p_i}{\sum_{p_i \in P} w(p_i)} \tag{3}$$

where $p_i = \{x_i, y_i, z_i\} \in R^3$, and $w(p_i)$ is the weight of the point expressed in Equation (5).

$$w(p_i) = \exp\left(\frac{-d_i^2}{d_o^2}\right) \tag{4}$$

where d_i is the Euclidean distance from the point p_i to the fitting surface, and d_0 is an average distance of d_i.

$$\Delta r = |\text{res}_{i+1} - \text{res}_i| \leq \Delta res_0 = 0.001 \tag{5}$$

where res_i and res_{i+1} are the residual of iteration i and $i+1$, which is expressed in Equation (6).

Component	TP	FP	FN	Comp	Corr	F1-score
RANSAC vs GT[*]						
Ballast wall	413,423	1,184	22,934	94.7%	99.7%	0.972
Breast wall	517,487	32	28,294	94.8%	100.0%	0.973
Wing wall	3,383,824	13,880	204,577	94.3%	99.6%	0.969
VRG vs GT						
Ballast wall	428,145	1,667	8,212	98.1%	99.6%	0.989
Breast wall	534,466	11,285	11,315	97.9%	97.9%	0.979
Wing wall	3,579,463	31,574	8,938	99.8%	99.1%	0.994

Note(s): [*] Point clouds of Segment 1 and 4 (Figure 2a) are considered as the points of the wing wall for evaluation

Table 1.
Summarized comparison of surface extraction based RANSAC and VRG vs GT

$$\text{res}_i = \sqrt{\frac{1}{|d_i|} \sum_{i=1}^{N} d_i^2} \tag{6}$$

where d_i is Euclidean distance from the point p_i to the fitting plane $S_{\text{fit}} = (p_0, n)$ (Equation 7).

$$d_i = \frac{(x_i - x_0)n_x + (y_i - y_0)n_y + (z_i - z_0)n_z}{\sqrt{n_x^2 + n_y^2 + n_z^2}} \tag{7}$$

For the second case, contextual knowledge derived from a design concept about the abutment components is used to determine their as-design surfaces. In the bridge design, the ballast and breast walls are perpendicular to the wing wall. As edges of the component connected to adjacent components are stiff, areas surrounding the edges are non-deformation. These areas can be selected to determine the surface representing an as-design status of the component. To get the surface determination from GT, points in the vicinity of the edges of a given component are extracted. The process starts with the points of the adjoined component to search the closest points within the given component, where the distances between the points of two surfaces are no larger than the predefined buffer (d_{buffer}). In this study, the buffer $d_{\text{buffer}} = 0.2$ m is empirically selected. Resulted extraction of the points of these areas is shown in Figure 3. Finally, rPCA (Equations 2–7) is employed to determine the as-design reference surface $S_{\text{ref,design}}$. Notably, for the breast wall, the bottom and top edges are also connected to other surfaces, while the right edge is not considered because a part of the breast wall was captured.

The resulting identification of the reference surface $S_{\text{ref,fit}}$ and $S_{\text{ref,design}}$ is shown in Table 2. A large root means square error (RMSE) of a fitting plane for the wing wall for the first case implies the wall is subjected to large deformation. Distances from the points of the abutment to the reference surface ($S_{\text{ref,fit}}$ and $S_{\text{ref,design}}$) are computed (Equation 7). The resulting deformations are illustrated in Figures 4 and 5.

In each case, patterns of deformations based on RANSAC and VRG are nearly similar, while the maximum values are slightly different. For example, minimum and maximum deformations differ 1.26 mm (RANSAC vs VRG) and 1.87 mm (RANSAC vs VRG) for the reference surface $S_{\text{ref,fit}}$, and 5.74 mm (RANSAC vs VRG) and -2.52 mm (RANSAC vs VRG) for the reference surface $S_{\text{ref,design}}$ (Figures 4 and 5, and Table 3). That implies that although there is different accuracy of surface extraction between RANSAC and VRG, differences of resulting deformations based on RANSAC and VRG are still minor. However, as RANSAC misses extracting points on the surface, the critical deformations are also excluded (Figures 4 and 5). Importantly, by using a fitting plane as the reference surface S_{ref}, the deformations of the abutment components appear as unreliable results (Figure 4). For example, there are large
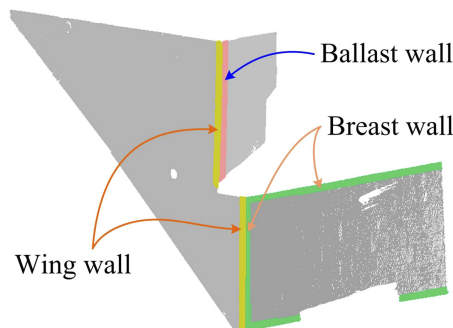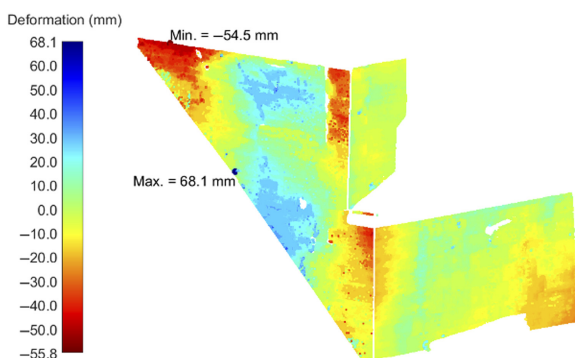

Figure 3.
Extract areas used to determine the as-design surfaces of the abutment components

deformations at edges adjoined to the ballast and breast walls for the wing wall, which is unrealistic. Moreover, there is no deformation at the middle of the wing wall, while other areas are subjected to deformations.

On the other hand, the approach to determine the reference surface–based contextual knowledge gives realisable deformation. For the wing wall, deformations increase for the part

Component	$p_0 = (x_0, y_0, z_0)$	$n = (n_x, n_y, n_z)$	RMSE (mm)
$S_{ref,fit}$			
Ballast wall	(9.956, 0.681, 6.734)	(−0.141, −0.99, −0.008)	3.6
Breast wall	(11.62, −0.791, 1.322)	(−0.146, −0.989, 0.017)	8.0
Winging wall	(9.005, 3.248, 4.941)	(−0.991, 0.128, 0.025)	17.0
$S_{ref,design}$			
Ballast wall	(8.880, 0.835, 6.191)	(−0.128, −0.992, −0.006)	2.7
Breast wall	(9.404, −0.459, 1.209)	(−0.148, −0.989, 0.018)	8.2
Winging wall	(8.626, 0.414, 3.783)	(−0.994, 0.103, 0.031)	3.8

Table 2.
Parameters of the
reference surface

Deformations based on RANSAC
(a)
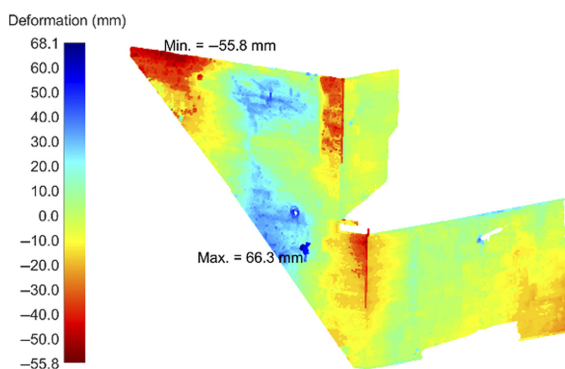
Deformations based on VRG
(b)

Figure 4.
Deformations based
$S_{ref,fit}$

Deformations based on RANSAC

(a)
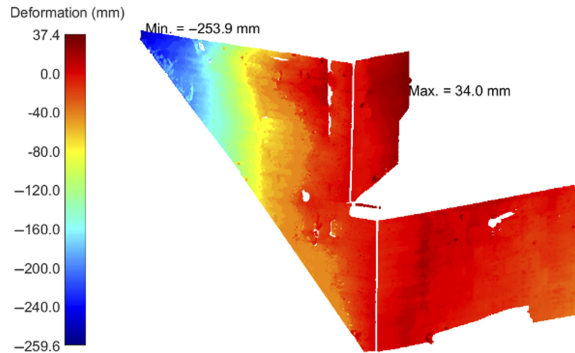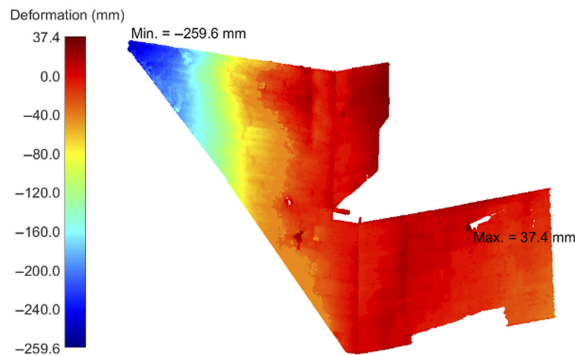
Deformations based on VRG

(b)

Figure 5.
Deformations based
$S_{ref,design}$

		$S_{ref,fit}$					$S_{ref,design}$				
Component	Abs. mean	Mean	Std	Min	Max	Abs. mean	Mean	Std	Min	Max
Surfaces derived from RANSAC										
Ballast wall	2.8	−0.8	3.4	−21.5	28.7	10.7	9.8	10.2	−13.4	34.0
Breast wall	5.9	−2.9	7.0	−25.9	27.4	6.9	−0.9	9.0	−38.5	30.0
Wing wall	14.1	0.6	16.8	−54.5	68.1	54.3	−53.9	55.0	−253.9	27.5
Surfaces derived from VRG										
Ballast wall	2.9	−0.7	3.5	−38.0	27.9	10.3	9.2	10.2	−37.2	34.0
Breast wall	6.2	−3.0	7.4	−28.4	38.0	7.0	−0.8	9.0	−39.4	37.4
Wing wall	14.3	0.0	17.0	−55.8	66.3	53.8	−53.3	55.9	−259.6	34.0

Table 3.
Statistical quantities of
deformations from
different reference
surfaces (unit = mm)

away from the ballast and breast walls because the wing wall behaves similar to the cantilever beam, which is fixed at the edges connected to the ballast and breast walls (Figure 5). Moreover, there is no deformation around the edges of the breast wall, while small deformations are found away from the edges, which is due to lateral pressure load. Therefore, it can be concluded that the reference surface $S_{ref,fit}$ based on a fitting plane, may not be used for deformation measurement, particularly when the surface is subjected to large deformation.
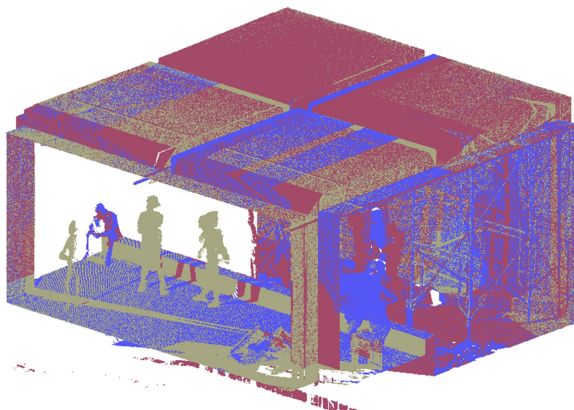
4.2 Deformation of the building slabs

An office building on Pham Ngu Lao st., Vietnam, was selected to be scanned by a Trimble TX8 with a maximum scanning range of from 0.6 m to 120 m (a range systematic error less than 2 mm) and an angular accuracy of 80 μrad in both vertical and horizontal (Trimble, 2020b). A point spacing of 11.3 mm at a range of 30 m and a total of ten scan stations were established to capture an interior storey with maximizing data coverage (Figure 6a). The point clouds were registered by the Trimble RealWork software v11.2 (Trimble, 2020a) with a registration error of about 1.57 mm. In this case, a part of the building ceiling is selected, which is only slabs over one span of a ground storey about 7.2 m wide and 7.2 m long, supported by the primary and secondary beams (Figure 6b). A subset includes 7.6 million data points of scanning stations 7, 8 and 9.

This case study investigates the impact of data quality due to registration (*Issue 1*), the quality of the surface extraction (*Issue 2*) on measuring vertical displacements of ceiling slabs and available outlier and noisy data (*Issue 4*). For *Issue 1*, data quality underlying a registration error is examined by comparing slab vertical displacements based on the point clouds from single and multiple scanning stations (SS and MS). Similar to case study 1, for *Issue 2*, RANSAC (Schnabel *et al.*, 2007) and CRG (Truong-Hong and Lindenbergh, 2020) are employed to extract data points of the ceiling slabs. Moreover, for minimizing impact of
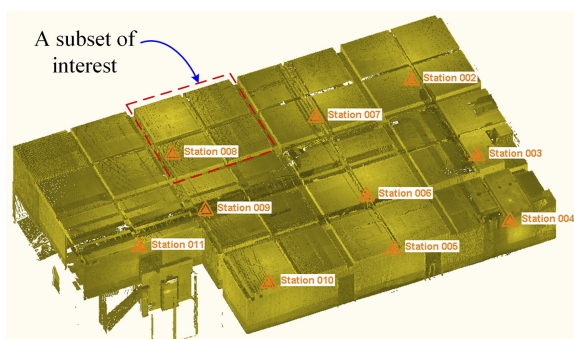
Point clouds of a building
(a)

(*) Points are rendered according to scan stations
A sub-set for measuring slab deformation
(b)

outlier points available in resulting segmentation, a moving smooth method with a spatial interval is applied to vertical displacements of sections of the slabs (*Issue 4*).

To extract data points of the ceiling slabs, for RANSAC, input parameters include $no\_ptc_{min} = 5,000$ points, $\varepsilon_{max} = 5$ mm, $\alpha_{max} = 2.5$ degrees, and $\beta = 0.5$, while parameters for CRG are $cs_O = 0.5$ m, $\alpha_O = 2.5$ degrees, $d_0 = 5$ mm and $res_0 = 5$ mm. These parameters are selected through several trials to get the best results. Both methods can extract the point clouds of the ceiling slabs properly (Figures 7a and b). Similar to case study 1, quantitative evaluation including Comp., Corr. and F1-score are used to interpret the quality of surface extraction from those methods comparing to GT (Figure 7c), which is manually extraction from the subset consisting of data points of scanning stations 7, 8 and 9 (Table 4). The point-based evaluation shows that CRG extracts data points of the ceiling slabs slightly better than RANSAC, where F1-score are 0.95 (RANSAC) and 0.99 (CRG) (Table 4).

For computing vertical displacements of ceiling slabs, the reference surface $S_{ref,i}$ ($i = [1;4]$) of each ceiling slab (CS_i) is first determined. Based on contextual knowledge, the ceiling slab CS_i supported by primary and secondary beams are fixed at intersection edges between the ceiling slab and the beams. Aiming to determine these intersection edges, point clouds of the ceiling slab CS_i and of the vicinity are decomposed into 2D cells ($C = \{c_i, i = [1; N_c]\}$) in x and y directions, which is similar to the first step of CRG (Truong-Hong and Lindenbergh, 2020) (Figure 8a). Next, cells are classified into boundary cells ($c_{ext,i} \in C$) located on the slab
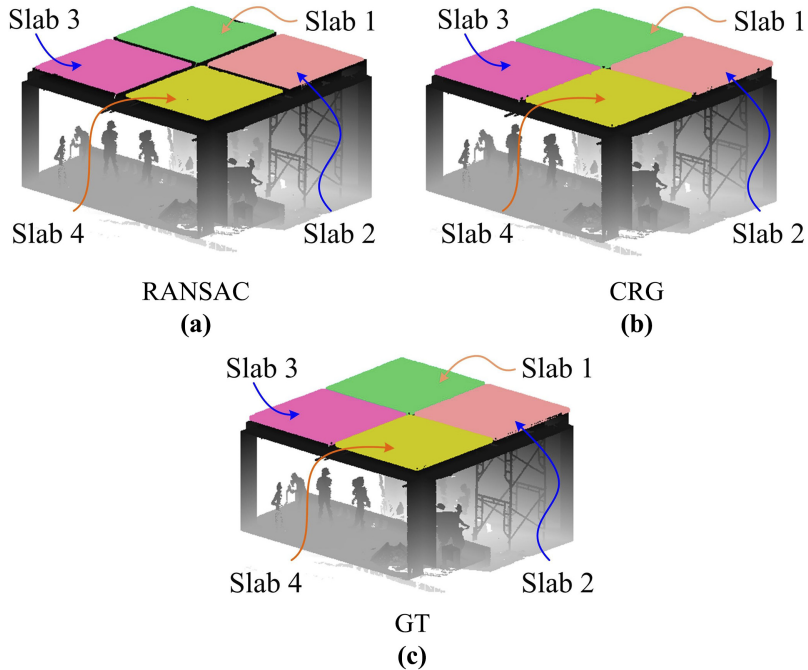

Figure 7.
Point clouds of ceiling slabs from RANSAC, CRG and GT overlaid input data

Quantitative	TP	FP	FN	Comp	Corr	F1-score
RANSAC vs GT	1,713,578	4,033	188,980	90.1%	99.8%	0.95
CRG vs GT	1,876,199	13,878	26,359	98.6%	99.3%	0.99

Table 4.
Evaluation of RANSAC and CRG

Decompose point clouds into 2D cells
(a)
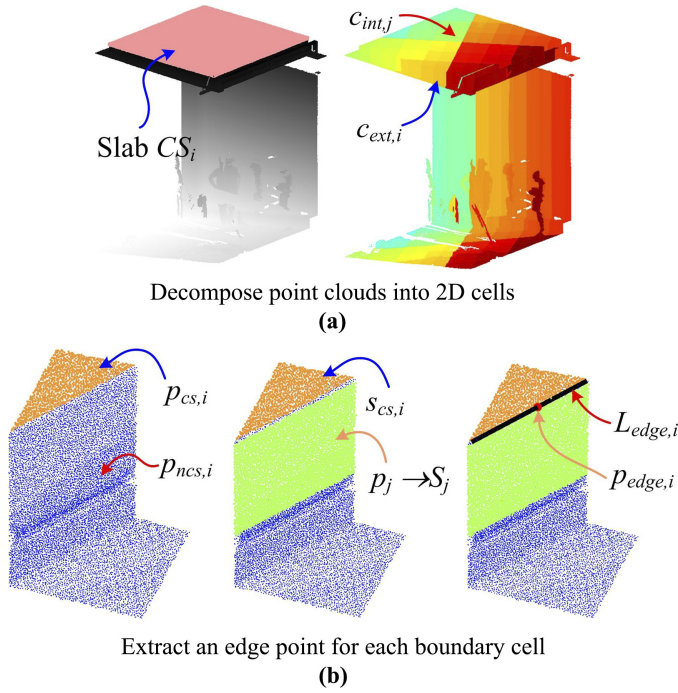
Extract an edge point for each boundary cell
(b)

boundaries and interior cells ($c_{int,j} \in C$). For each boundary cell $c_{ext,i}$, points ($p_i \in c_{ext,i}$) are separated into two groups: the slab points, $p_{cs,i}$ and non-slab points $p_{ncs,i}$, where $p_i = p_{cs,i} \cup p_{ncs,i}$ and $p_{cs,i} \neq \varnothing$ (Figure 8a). Subsequently, a point-based region growing proposed by (Rabbani *et al.*, 2006) was employed to segment the points $p_{ncs,i}$ into a set of regions $R = \{R_j, j = [1;N_R]\}$. The region $R_j = \{p_j\}$ is considered as a vertical surface of a supported beam of the ceiling slab CS_i if the fitting plane (S_j) of the region R_j are (1) perpendicular to the local surface $s_{cs,i}$ of the ceiling slab and (2) the closest to the ceiling slab CS_i (Figure 8b). In this study, rPCA (Equations 2–7) is used to determine $s_{cs,i}$ and S_j. Additionally, an intersection line ($L_{edge,i}$) between $s_{cs,i}$ and S_j is determined, and the middle point of the intersection line segment is considered as an edge point $p_{edge,i}$ (Figure 8b). Finally, the reference surface $S_{ref,i}$ is a fitting plane though edge points ($p_{edge} = \{p_{edge,i}\}$) of ceiling slab CS_i by using *rPCA* (Equations 2–7). Resulting reference surfaces of the ceiling slabs are present in Table 5. For details of a procedure of extracting the reference surface $S_{ref,i}$, one can refer to (Truong-Hong and Lindenbergh, 2020). Importantly, GT point clouds of the ceiling slabs are used as input data to determine the edge points in this study.

A vertical displacement at a point $p_i \in CS_i$ is defined as an orthogonal distance from the point p_i to the reference surface $S_{ref,i}$ (Equation 7). Resulting vertical displacements based on the slab points derived from GT, RANSAC and CRG are shown in Figure 9, while statistical quantities of the vertical displacements of each ceiling slab are present in Table 6. Patterns of vertical displacements are similar (Figure 9), but the minimum and maximum vertical displacements are different (Table 6). Notably, the vertical displacements from CRG are highly consistent with those from GT, where averaged differences of absolute mean and mean are respectively −0.03 and 0.05 mm (Table 6), while these values between RANSAC and GT are 0.07 and 0.10 mm. However, there is a large difference in the maximum and minimum values between CRG and GT. For example, the maximum vertical displacements are 31.2 mm for GT and 18.9 mm for CRG. This implies that outlier points may still be available in GT.

In the building ceiling slab, large vertical displacements often occur at the middle spans, and vertical displacements along four sections are observed (Figure 9). As noisy data points are inevitable, a moving average method is employed to smooth vertical displacements, in which an interval space (w) of 0.05 m is used to compute the vertical displacement at the predefined location p_i along the section (Equation 8).

$$\bar{\delta}_{\text{vert},i} = \frac{\sum \delta_j}{|\delta_j|} \tag{8}$$
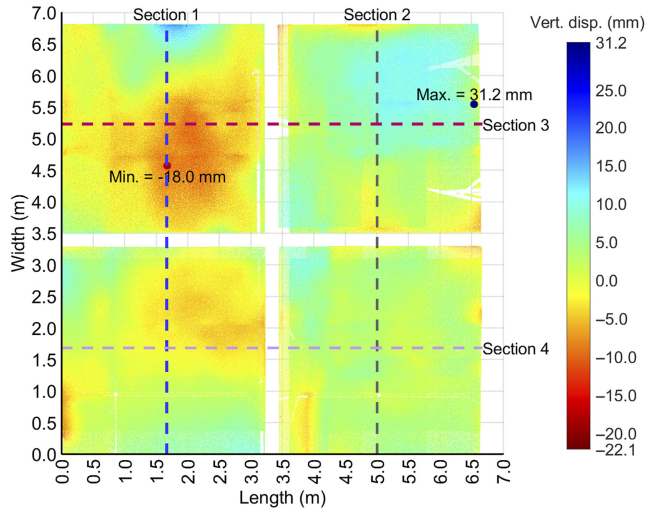
GT
(a)
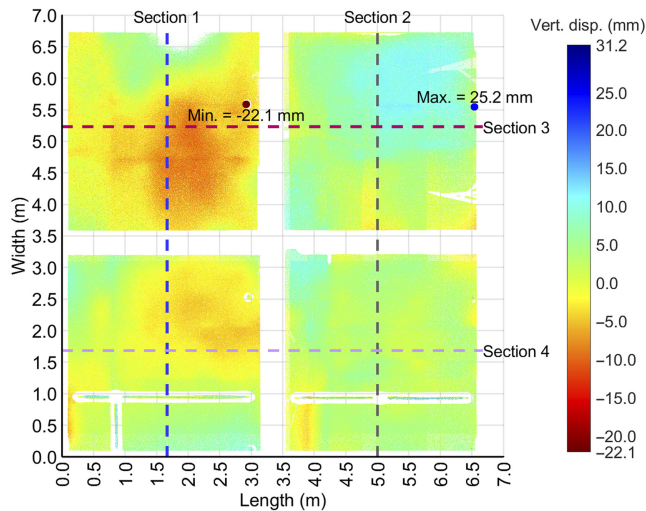
RANSAC
(b)

Figure 9.
Vertical displacements of the ceiling slabs derived from GT, RANSAC and CRG

CRG

(c)
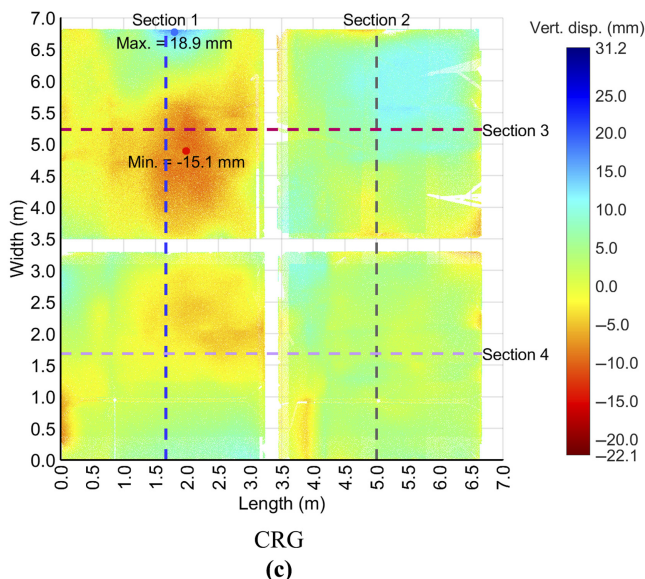
Figure 9.

Note(s): Positive and negative values respectively illustrate sagging and hogging

Slab	$p_0 = (x_0, y_0, z_0)$	$n = (n_x, n_y, n_z)$	RMSE (mm)
Slab 1	(9.868, 13.231, 1.825)	(−0.007, 0.005, 1.000)	5.0
Slab 2	(9.868, 13.231, 1.825)	(−0.007, 0.005, 1.000)	3.0
Slab 3	(6.831, 14.985, 1.831)	(−0.006, 0.003, −1.000)	4.0
Slab 4	(8.130, 10.308, 1.835)	(0.004, 0.004, 1.000)	3.0

Table 5.
Parameters of
reference surfaces
$S_{ref,i} = (p_0, n)$ of the
ceiling slabs

Component	Abs. Mean	Mean	Std	Min	Max
GT					
Slab 1	4.8	−3.3	4.9	−18.0	23.6
Slab 2	5.2	4.9	3.7	−11.6	31.2
Slab 3	2.8	−0.2	3.3	−11.8	13.7
Slab 4	2.8	2.5	2.0	−8.2	13.8
RANSAC					
Slab 1	4.9	−4.0	4.3	−22.1	8.0
Slab 2	5.4	5.2	3.5	−7.0	25.2
Slab 3	2.8	−0.3	3.4	−10.0	17.3
Slab 4	2.9	2.7	2.0	−7.3	19.3
CRG					
Slab 1	4.7	−3.2	4.8	−15.1	18.9
Slab 2	5.2	4.9	3.6	−8.7	14.1
Slab 3	2.8	−0.2	3.4	−10.6	15.7
Slab 4	2.8	2.5	2.0	−7.8	13.9

Table 6.
Statistical quantities of
vertical displacements
from GT, RANSAC and
CRG (unit = mm)

where δ_j is a vertical displacement at the data point p_j, $|\;|$ denotes the number of points within the interval space w, which is determined based on Equation (9).

$$\begin{cases} p_i.y - \dfrac{w}{2} \le p_j.y \le p_i.y + \dfrac{w}{2} & \text{for Section 1 and 2} \\[2mm] p_i.x - \dfrac{w}{2} \le p_j.x \le p_i.x + \dfrac{w}{2} & \text{for Section 3 and 4} \end{cases} \tag{9}$$

where suffixes ".x and.y" donate x- and y-coordinates of the points. Notably, the predefined locations $p = \{p_i\}$ are linearly generated along the section with the interval space $w = 0.05$ m.

Results of vertical displacements along four sections are shown in Figures 10 and 11. Generally, deformation shapes from GT, RANSAC and CRG are similar, but outlier points are
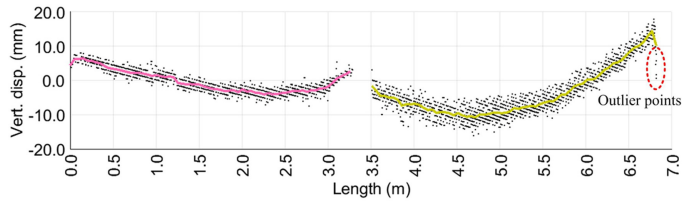
(a) Section 1
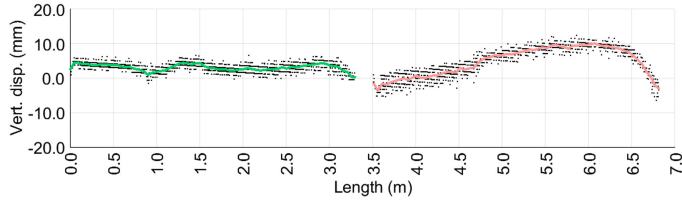
(b) Section 2
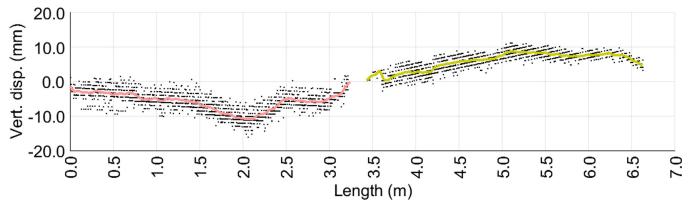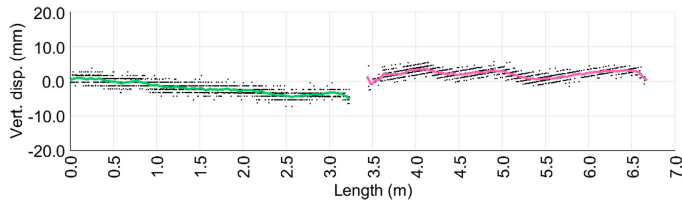
(c) Section 3

(d) Section 4

Figure 10.
Vertical displacements along sections-based GT

still available in GT ([Figure 10a](#)) and RANSAC ([Figure 11c](#)). However, CRG can eliminate outlier points and trim a few noisy data points. Finally, comparing the vertical displacements based on the point clouds derived from RANSAC and CRG against those based GT shows that results-based CRG highly agree with those from GT ([Table 7](#)). Although an average of the mean vertical displacements is 0.05 mm (RANSAC vs GT) and 0.02 mm (CRG vs GT), the averaged minimum/maximum vertical displacements are 1.05 mm/0.40 mm (RANSAC vs GT), and 0.84 mm/0.015 mm (CRG vs GT). Results prove that although the performance of RANSAC in extracting the points of the ceiling slabs is lower than that of CRG, it would not cause a significant difference in measuring the vertical displacements. However, the vertical displacements at cross-sections along sections vary about 10 mm ([Figures 10a and c, 11a and c,](#)
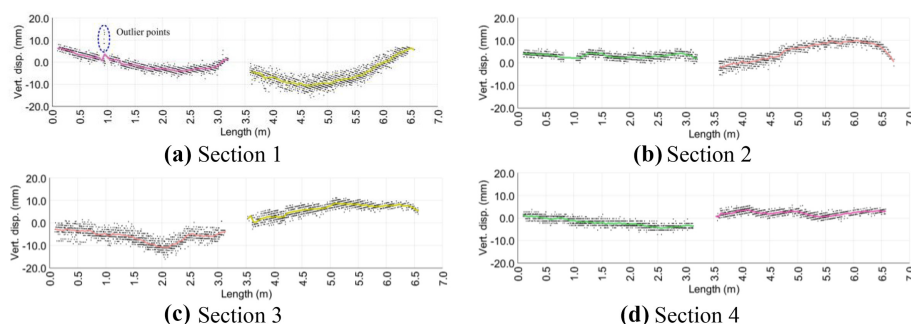

(a) Section 1 (b) Section 2

(c) Section 3 (d) Section 4

Figure 11.
Vertical displacements
along sections-based
RANSAC

Methods	Mean	Std	Min	Max	Mean	Std	Min	Max
	Section 1 - Slab 1				*Section 1 - Slab 3*			
GT	−5.0	5.4	−10.8	9.6	−0.5	3.1	−4.1	6.5
RANSAC	−5.2	5.0	−10.8	6.4	−0.4	3.2	−4.1	6.5
CRG	−4.9	5.4	−10.6	9.4	−0.5	3.1	−4.1	6.5
RANSAC vs GT	−0.2	0.6	−3.9	0.0	0.0	0.3	−1.0	2.4
CRG vs GT	0.1	0.2	−0.2	1.5	0.0	0.0	−0.3	0.1
	Section 2 - Slab 2				*Section 2 - Slab 4*			
GT	5.2	3.9	−1.9	10.1	3.3	0.7	2.1	4.4
RANSAC	5.2	3.8	−1.9	10.1	3.3	0.7	2.1	4.4
CRG	5.2	3.8	−1.4	10.1	3.3	0.7	2.1	4.4
RANSAC vs GT	0.0	0.1	0.0	0.5	0.0	0.0	−0.3	0.1
CRG vs GT	0.0	0.1	0.0	0.4	0.0	0.0	0.0	0.0
	Section 3 - Slab 1				*Section 3 - Slab 2*			
GT	−5.9	2.4	−10.9	−2.7	6.1	2.3	0.4	8.7
RANSAC	−5.9	2.4	−10.9	−2.6	6.1	2.3	0.4	8.7
CRG	−5.9	2.4	−10.6	−2.3	6.1	2.3	0.4	8.7
RANSAC vs GT	0.0	0.1	−0.4	0.1	0.0	0.0	−0.1	0.0
CRG vs GT	0.0	0.2	−0.5	0.6	0.0	0.0	0.0	0.0
	Section 4 - Slab 3				*Section 4 - Slab 4*			
GT	−2.0	1.6	−4.5	1.0	2.3	0.8	0.6	3.6
RANSAC	−2.0	1.6	−4.5	1.3	2.3	0.8	0.6	3.6
CRG	−2.0	1.6	−4.5	1.0	2.3	0.8	0.6	3.6
RANSAC vs GT	0.0	0.0	0.0	0.4	0.0	0.1	0.0	0.4
CRG vs GT	0.0	0.0	0.0	0.0	0.0	0.0	0.0	0.0

Table 7.
Statistical quantities of
vertical displacements
(unit: mm)

(a) Section 1

(b) Section 2

(c) Section 3

(d) Section 4
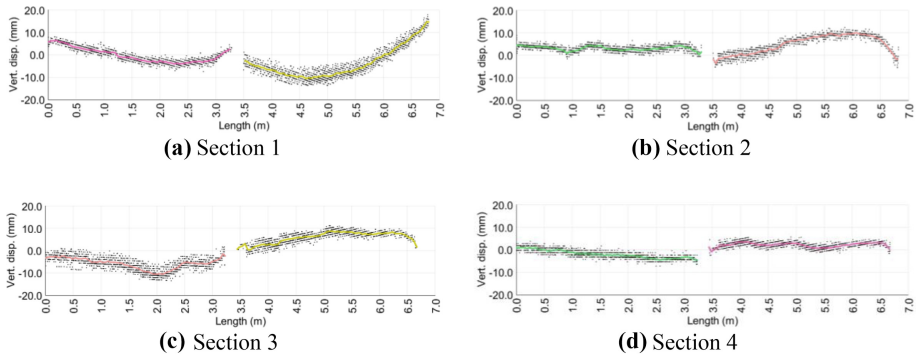
and 12a and c), which reflects that the data quality is relatively low, which may be caused by a sensor and/or a registration error.

Addressing the impact of data quality on vertical displacement measurement (*Issue 1*), vertical displacements based on one scanning station (SS) point clouds are compared to those based on multiple scanning station (MS) ones. In this case study, the scanning station 8 below these ceiling slabs has a short scanning distance and small incidence angle compared to other stations, which is expected to give the best quality of the point clouds. As CRG is better than RANSAC in surface extraction from the MS subset, only CRG is used to extract the point clouds of the ceiling slab from the SS subset consisting of 3.7 million points, in which input parameters are similar to ones applying for the MS subset. Subsequently, reference surfaces ($S_{ref,i}$) for each ceiling slab (CS_i) are estimated from edge points extracted from the SS subset (Figure 13a and Table 8). The reference surfaces from the SS subset are identical to those based on the MS subset.

Finally, vertical displacements of the slabs are computed by using Equation (7), and results are illustrated in Figure 13b. The vertical displacements based on the SS subset highly agree with those based on the MS subset. This trend is also observed through the vertical displacements along four sections (Figure 14). Differences of mean vertical displacements between CRG-MS and CRG-SS are mostly less than 0.6 mm (Table 9), while differences of maximum vertical displacements are no larger than 1.6 mm (14.7 mm for CRG-MS vs 13.1 mm for CRG-SS in Slab 1 along Section 1). Moreover, average noise levels of MS and SS subsets
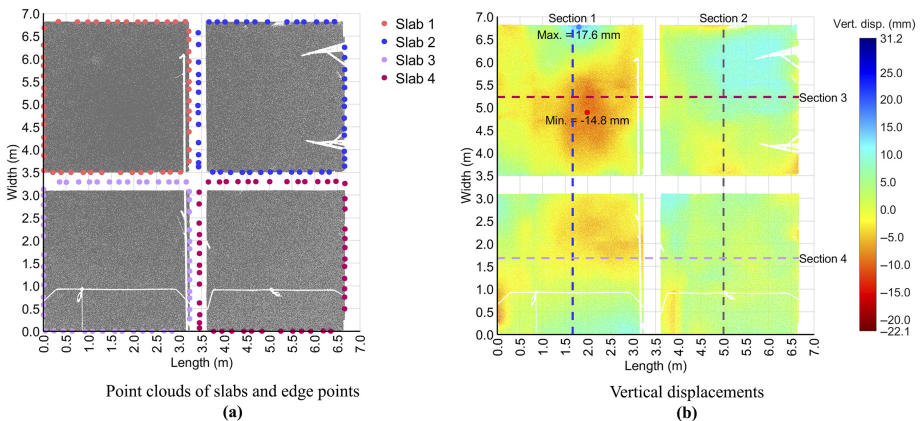
Point clouds of slabs and edge points

(a)

Vertical displacements

(b)

are respectively 1.0 mm ($std = 0.88$ mm) and 1.0 mm ($std = 0.86$ mm) (Figure 15). The upper bound of the noise levels for the 95% confidence interval is 1.13 mm (the MS subset) and 1.16 mm (the SS subset) when using Weibull distribution. Thus, with a magnitude order of the noise level of the subsets, it can be arguably concluded that for this case, the noise would be strongly affected on vertical displacements, while a registration error of 1.57 mm causes a minor effect. This finding was also reported by Pesci *et al.* (2013). Notably, the noise is measured as the distance from the points to the fitting plane through its neighbouring points, which are 20 nearest neighbouring points used in this study. For details on computing noise, one can refer to Soudarissanane *et al.* (2011), Laefer *et al.* (2014).

4.3 Deformation of steel frame
As part of tank inspection (American Petroleum Institute, 2014), a steel frame supporting the tank roof must be assessed, in which deformation of the girders is a part of the assessment. In
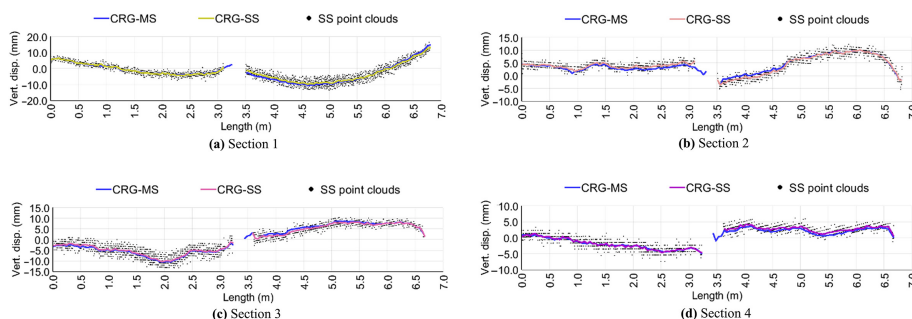
Figure 14.
Averaged vertical displacements along four sections from the SS subset

Slab	$p_0 = (x_0, y_0, z_0)$	$n = (n_x, n_y, n_z)$	RMSE (mm)
Slab 1	(9.802, 13.237, 1.824)	(−0.007, 0.006, 1.000)	5.0
Slab 2	(7.795, 10.345, 1.837)	(−0.004, −0.004, −1.000)	3.0
Slab 3	(6.796, 15.049, 1.832)	(−0.006, 0.003, −1.000)	5.0
Slab 4	(5.006, 12.118, 1.840)	(−0.003, −0.003, −1.000)	3.0

Table 8.
Parameters of reference surfaces ($S_{ref} = (p_0, n)$) of the ceiling slabs

Methods	Mean	Std	Min	Max	Mean	Std	Min	Max
	Section 1 - Slab 1				*Section 1 - Slab 3*			
CRG-SS	−3.3	6.2	−9.9	13.1	−0.3	3.4	−4.4	6.5
CRG-S vs CRG-MS	0.3	0.8	−1.8	1.6	−0.1	0.3	−0.7	1.2
	Section 2 - Slab 2				*Section 2 - Slab 4*			
CRG-SS	4.4	4.4	−3.6	10.1	3.9	0.8	1.7	5.7
CRG-S vs CRG-MS	−0.4	0.5	−1.5	0.4	0.6	0.5	−0.1	2.5
	Section 3 - Slab 1				*Section 3 - Slab 2*			
CRG-SS	−5.3	2.5	−10.3	−1.1	5.6	2.5	0.4	8.2
CRG-S vs CRG-MS	0.4	0.2	0.2	1.2	−0.4	0.4	−1.3	0.3
	Section 4 - Slab 3				*Section 4 - Slab 4*			
CRG-SS	−2.0	1.7	−4.7	1.3	2.8	0.8	0.5	4.2
CRG-S vs CRG-MS	0.0	0.3	−0.6	0.6	0.6	0.2	0.1	1.1
Note(s): CRG-MS is CRG presented in Table 7								

Table 9.
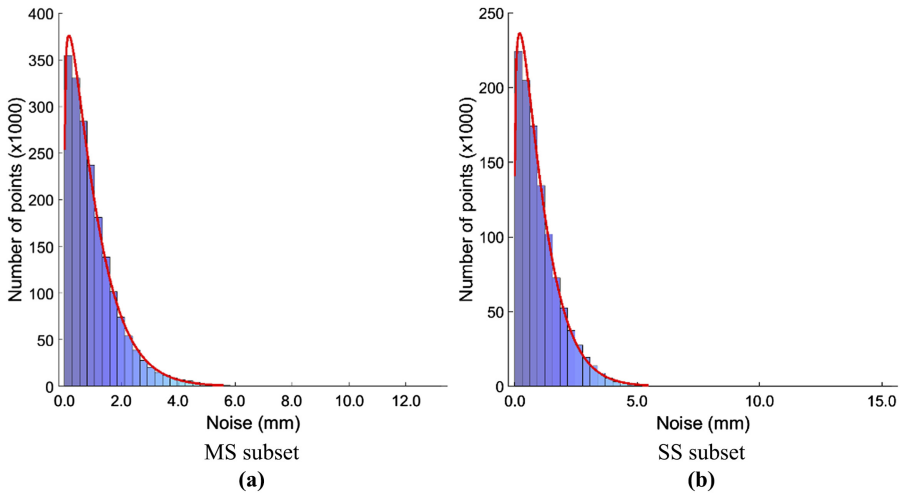Statistical quantities of vertical displacements along sections from the SS subset (unit = mm)[*]

this case study, the oil tank located in Alberta in Canada, which is 27.4 m in diameter and 14.6 m in height, was used. The steel frame is located at an elevation about 15 m from the tank floor. Faro Focus X130 (Faro, 2020b) with a scanning range from 0.6 m to 130 m, a range error of ± 2 mm was used to capture the steel frame from an averaged distance of 15.0 m. Due to the occlusion, to obtain full coverage point clouds of the steel frame, a total of five scanning stations were set up, and they captured the structure with the sampling step by 6.136 mm at a measurement range of 10 m (Figure 16a). The point clouds from different scanning stations were registered by using Faro PointSense software version 18.5 (Faro, 2020a) with a mean point error of 0.9 mm and a maximum point error of 2.1 mm. As this study aims to demonstrate factors affecting the deformation measurement–based laser scanning point clouds, only data points of a girder of interest were selected (Figure 16b). The complete point cloud of the girder comes from three scanning stations 2, 4 and 5. Subsequently, the point clouds of the girder of interest and its adjoining structures (e.g. column heads) were manually extracted within Cloudcompare (2021).

Case study 2 shows that the quality (due to a registration error) of a point cloud would affect resulting vertical displacements. This case study demonstrates the effectiveness of the point cloud quality (*Issue 1*), selecting segmentation methods (*Issue 2*) and available outlier and noisy data (*Issue 4*). Moreover, an impact of mixed pixels (Wang *et al.*, 2016) during capturing steel
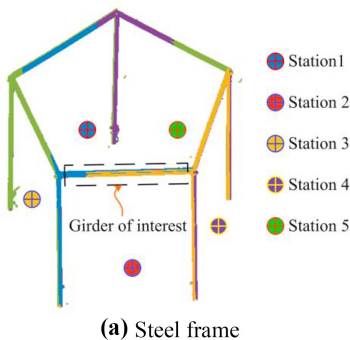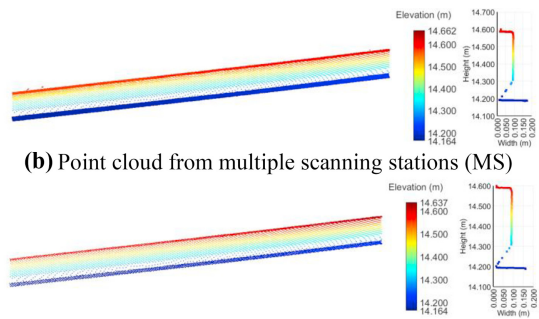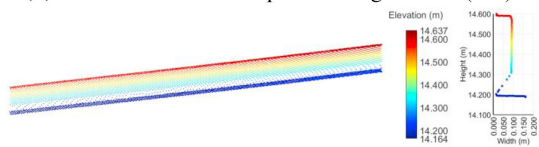
structures is also included in *Issue 4*. Two subsets (1) multiple scan stations (MS) (including stations 2, 4 and 5), and (2) a scan station 5 (SS) are used to measure vertical displacements of the girder (Figure 16b and c). The use of MS subsets reflects that in practice, the complete point cloud of a structural member is not sometimes obtained from one scanning station, while an SS subset can give insight impact of a registration error on deformation measurements. Notably, Station 5 is selected as its point cloud is given the best coverage of the girder.

Both RANSAC (Schnabel *et al.*, 2007) and VRG (Vo *et al.*, 2015) are employed to extract data points of the girder surfaces. As the vertical displacement of the girder is the main interest, the segmentation aims to extract a point cloud of the bottom surface ($S_{girder,bot}$) of the girder. For RANSAC, input parameters are *min_ptc* = 500 points, ε_{max} = 10 mm, α = 5.0 degrees and β = 0.2, while for VRG the parameters are vs_0 = 0.1 m, α_0 = 5.0 degrees, d_0 = 5 mm and res_0 = 5 mm. Notably, in RANSAC, a normal vector of each point is a normal plane fitted through 20 nearest neighbour points. Results of segmentation showed that RANSAC and VRG successfully extract data points of the bottom surface $S_{girder,bot}$ (Figure 17). Moreover, a visualisation evaluation shows that under-segmentation occurs in $S_{girder,bot}$ derived from the SS subset (Figure 17d and e). Quantitative evaluation by comparing points of $S_{girder,bot}$ from RANSAC and VRG against GT are shown in Table 10. It is shown that for the MS subset, both methods extract $S_{girder,bot}$ with higher accuracy from the MS subset than from the SS subset. For MS subset, Comp. and *F*-1 score are respectively no
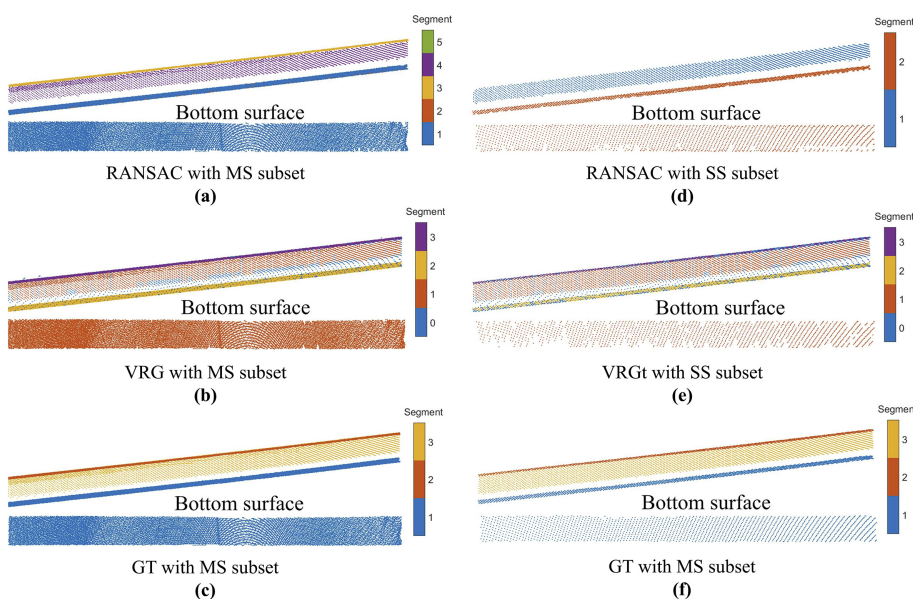

Figure 17.
Point clouds of
surfaces of the girder
from various methods

Component	TP	FP	FN	Comp	Corr	F1-score
GT vs RANSAC-MS	19,134	125	215	98.9%	99.4%	0.991
GT vs VRG-MS	19,214	91	135	99.3%	99.5%	0.994
GT vs RANSAC-SS	1,755	204	112	94.0%	89.6%	0.917
GT vs VRG-SS	1,533	76	334	82.1%	95.3%	0.882

Table 10.
Evaluation of
RANSAC and VRG for
MS and SS subsets

smaller than 98.9% and 0.991, while for the SS subset, they are no larger than 94.0% and 0.917 (Table 10). Interestingly, although VRG performs better than RANSAC for the MS subset, the opposite trend is found for the SS subset. This implies that a lower sampling step of the SS subset can affect the quality of a fitting plane within the voxel. Consequently, that would lead to under-segmentation.

As an initial surface or a reference surface, S_{ref} of the girder is not available, to compute vertical displacement, a surface through a set of points at two ends of the bottom surface $S_{girder,bot}$, is assumed to be the reference surface S_{ref}. This assumption is based on the reality that the girder was welded to the column, so two girder ends are being fixed. To do that, points within the buffer of 0.05 m from two ends of $S_{girder,bot}$ are extracted (Figure 18), and rPCA (Equations 2–7) is employed to fit the plane. In this case study, point clouds of $S_{girder,bot}$ from GT, estimate S_{ref} for the MS and SS subsets, and the results are shown in Table 11. There is a very slight difference between S_{ref} from two subsets, where the deviation between their normal is about 1 degree.

Additionally, vertical displacements of the girder are computed by Equation (7), which are orthogonal distances from points of $S_{girder,bot}$ to the corresponding reference surface S_{ref}. Results of vertical displacements for each point are shown in Figure 19. Generally, the vertical displacements based on RANSAC and VRG highly agree with those based on GT for both subsets (Table 12). Differences of absolution mean and mean of vertical displacements are no more than 0.5 mm for both subsets. However, there are significant differences in the minimum and maximum vertical displacements based on RANSAC. For the minimum vertical displacements, they are −13.3 mm (−26.4 mm for RANSAC-MS vs −13.2 mm for GT-MS) and −16.6 mm (−28.2 mm for RANSAC-SS vs −11.6 mm for GT-SS) (Table 12). A similar trend is

Table 11.
Parameters of reference surfaces [$S_{ref} = (p_0, n)$] of the bottom surface of the girder

Data	$p_0 = (x_0, y_0, z_0)$	$n = (n_x, n_y, n_z)$	RMSE (mm)
GT-MS	(2.294, 0.093, 14.190)	(−0.005, 0.01, 1.000)	1.0
GT-SS	(6.554, 0.083, 14.211)	(−0.005, 0.028, 1.000)	1.0

Table 12.
Statistical quantities of vertical displacements from GT, RANSAC and VRG (unit = mm)

Methods	Abs. Mean	Mean	Std	Min	Max	Abs. Mean	Mean	Std	Min	Max
		MS subset					SS subset			
GT	6.5	−6.5	3.1	−13.2	2.3	6.3	−6.2	3.3	−11.6	2.1
RANSAC	6.5	−6.5	3.2	−26.4	3.0	6.6	−6.2	4.3	−28.2	23.2
VRG	6.5	−6.5	3.1	−15.0	3.7	6.4	−6.4	3.3	−14.2	2.8
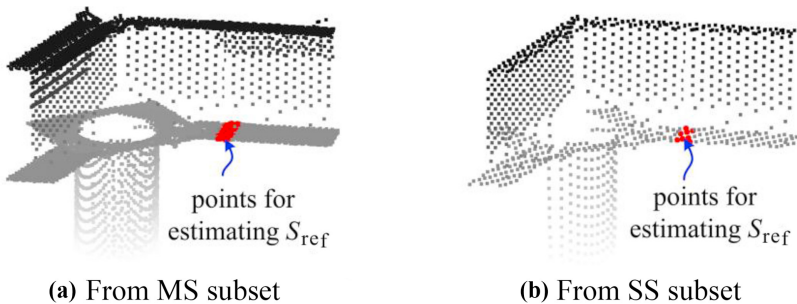
Figure 18.
Illustrated points within a buffer from the end of $S_{girder,bot}$ for estimating S_{ref}

(a) From MS subset   **(b)** From SS subset

Figure 19.
Vertical displacements
of the girder from MS
and SS subsets
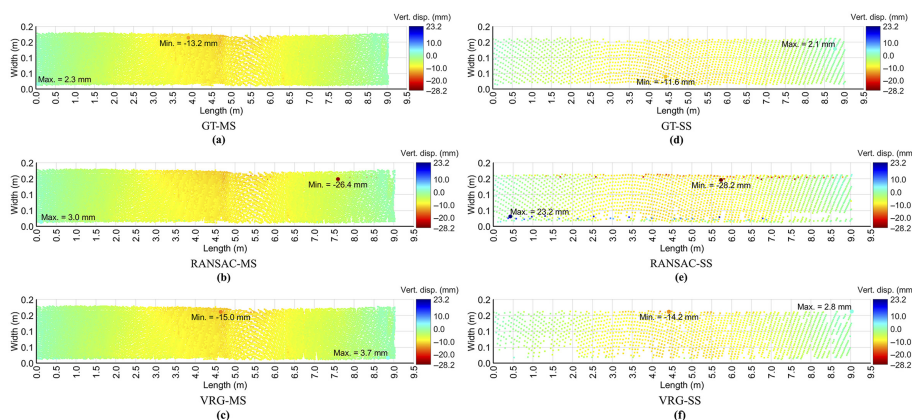
also found in the maximum vertical displacement from the SS subset with a difference of 21.1 mm (Figure 19 and Table 12). This implies that mixed pixels are still available around the edges of $S_{\text{girder,bot}}$ derived from RANSAC (Figure 20). This phenomenon is eliminated chiefly from resulting point clouds from VRG.

Figure 21 shows vertical displacements at a middle section of $S_{\text{girder,bot}}$ along a longitudinal direction of the girder and smooth vertical displacements by applying a moving average method presented in case study 2. Vertical displacements are nearly identical for all cases (Figure 21 and Table 13). Interestingly, differences of all statistical quantities are no larger than 0.4 mm for VRG vs GT with the SS subset. Moreover, there is a very slight difference between results-based MS and SS subsets, in which mean values of vertical displacements differ no more than 0.1 mm. Thus, once the mixed pixels are eliminated, the vertical displacements based on the MS and SS subsets are the same.

Similar to case study 2, noise levels of both subsets are similar, where the average noises are respectively 0.4 mm (std = 0.3 mm) for the MS subset and 0.4 mm (std = 0.3 mm) for the SS subset (Figure 22), while the upper bound of the noise levels corresponding to the 95%
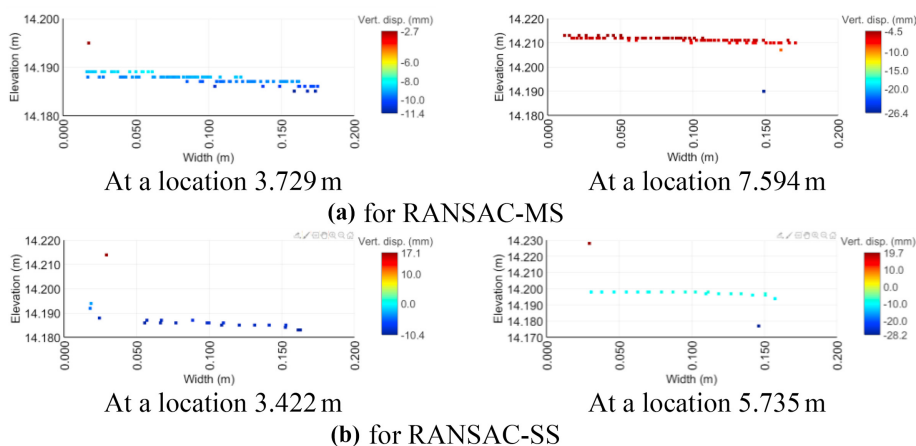

Note(s): *a location refers to Figure 19

Figure 20.
Illustrated mixed
pixels available in
$S_{\text{girder,bot}}$ derived from
RANSAC

Figure 21.
Vertical displacements
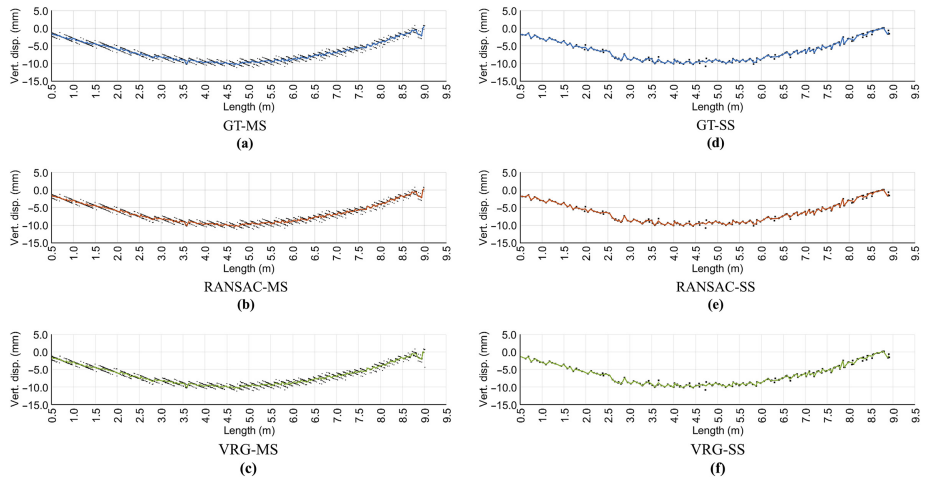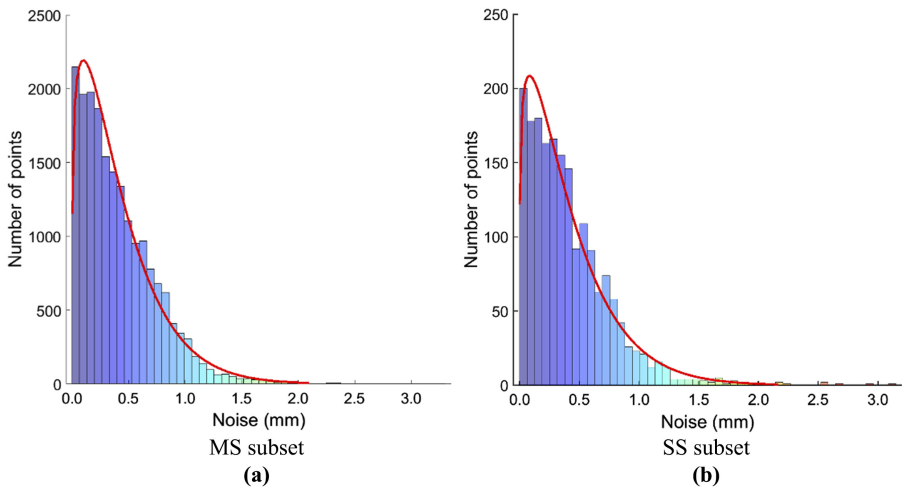of a middle section
along the girder

Figure 22.
Noise levels of MS and
SS subsets

confidence interval are 1.1 mm (the MS subset) and 1.1 mm (the SS subset) when using Weibull distribution. That can translate with high accuracy of a registration (the average registration error of 0.9 mm) in this case study, resulting deformation estimation does not get affected. Thus, the use of point clouds from multiple scanning stations would give accurate deformation of a structure. Notably, the local plane at a given point for computing the noise is determined from 20 nearest neighbouring points.

5. Discussions
The paper presents an application of terrestrial laser scanning point clouds to measure deformation for structural assessment. The deformation is defined as a distance between a point cloud representing a current surface and a reference surface S_{ref} representing the initial or non-deformed surface of the structure. Structural components of a bridge, building and storage

tank are used to demonstrate deformation measurement and investigate the impact of point cloud registration error, selected segmentation methods to extract a point cloud of a surface, selection of the reference surface S_{ref}, and available outlier, noisy data and/or mixed pixels.

Clearly, the reference surface plays a crucial role in computing the deformation. Case study 1 illustrates that the deformations of the abutment components are essentially different when different reference surfaces are applied. For example, the maximum lateral deformations of a wing wall increase from 54.36 mm to 254.15 mm for points of a surface derived from RANSAC when the reference surface based on a fitting plane ($S_{\text{ref,fit}}$) and a design concept ($S_{\text{ref,design}}$) are applied. Based on deformation distribution of the abutment components in case study 1, where unrealistic deformation appears in several areas of the surfaces, it can arguably conclude that the fitting plane based on the points of the surface may not be the reference surface when the structural surface is subjected to damage or large deformation. For example, RMSE of a fitting plane for the wing wall is 17.0 mm (Table 2). That is because the effects of point clouds of damage areas on a fitting plane cannot be eliminated although a robust fitting approach is applied. Therefore, $S_{\text{ref,design}}$ would be recommended. However, due to data quality or imperfect construction, $S_{\text{ref, design}}$ obtained from point clouds would differ from design documentations. For example, in principle, in the case study 2, points on slab edges should be coplanar, but results of fitting planes through their points show RMSE up to 5 mm (Tables 5 and 8). Moreover, as the complexity of a structure, the resulting segmentation based on RANSAC and CRG/VRG still includes data points of adjoined structures (Figure 21), and these points also impact estimating the reference surface.

Technically, RANSAC and CRG or VRG successfully extract point clouds of surfaces of structures. However, both are required to tune input parameters to obtain the best results (Vo et al., 2015). However, as RANSAC is a model-based method, the method is only suitable for the surface subjected to a small deformation, where the points on the deformed areas have distances to the model smaller than $\varepsilon_{\max}$. When the surface is subjected to large deformation, RANSAC can fail to extract complete points of the surface, where parts of the large deformation area are excluded. For example, in case study 1, RANSAC (Schnabel et al., 2007) segments the point cloud of the wing wall into two clusters, and point clouds of some areas also exclude (Figure 2). Moreover, resulting in point clouds based on RANSAC can contain outlier points or points of adjoined structures (Figure 11a), which can cause extreme deformations to be reported. On the other hand, as region growing–based methods are applicable for extracting a free-form surface (Vo et al., 2015), they are suitable for the structure surfaces subjected to arbitrary deformation. In most cases, CRG and VRG give higher accuracy in extracting the points of the surface than RANSAC. However, VRG would have a low performance when a low density of the point cloud is used, as shown in case study 3 (Figure 19f). Furthermore, VRG is also better than RANSAC in eliminating mixed pixels surrounding the edges of a steel structure (Figure 19). Except for outlier points, deformation of the structure-based data points derived from RANSAC and CRG/VRG are similar to ones from GT. Thus, to give reliable deformations of the structure based on the point cloud, one of the key points is to minimize outlier points in the surface data points.

| Methods | Mean | Std | Min | Max | Mean | Std | Min | Max |
			MS subset				SS subset	
GT	−6.3	3.0	−10.4	0.6	−6.4	3.1	−10.2	1.8
RANSAC	−6.3	3.0	−10.4	0.4	−6.4	3.1	−10.2	1.8
VRG	−6.3	3.0	−10.4	0.2	−6.4	3.1	−10.2	1.8
RANSAC vs GT	0.0	0.0	−0.1	0.0	0.0	0.0	0.0	0.0
VRG vs GT	0.0	0.0	−0.7	0.0	0.0	0.0	−0.1	0.4

Table 13.
Statistical quantities of vertical displacements from GT, RANSAC and CRG (unit = mm)

Mixed pixels, noise and a registration error of data points inevitably occur and are critical factors in measuring the deformation of a structure based on TLS data points. The registration error is completely removed when a point cloud of a single scanning station is used. However, that would not be generally applicable in practice because the complexity and size of the structure are restricted to obtain full coverage data of the structure from one scanning station. Thus, the registration error must be minimized. It can be seen that although point clouds from multiple scanning stations are used, the registration errors of 1.57 mm (case study 2) and 0.9 mm (case study 3) do not cause a negative impact on the resulting deformation.

Although CRG and VRG can partially reduce the availability of mixed pixels and noisy data points, point-based deformation can report extreme deformations at outmost points (either mixed pixels or outlier points), leading to an incorrect decision to be reported. Fortunately, as the mixed pixels mostly occur surrounding edges of the structure (Laefer *et al.*, 2014), the points within a buffer of the surface edges would be excluded. For example, when the points of the middle sections are used, the effects of the mixed pixels are eliminated (Figure 21). Alternative outlier removal techniques, for example, statistical outlier removal proposed by Rusu *et al.* (2008), would be used to remove the mixed pixels. However, data points of damaged areas, which are subjected to large deformation, can also be removed because their spatial information may be similar to the mixed pixels or outlier points. In addition, an effect of noisy data, where the large deformation to be reported at outlier points (Jafari *et al.*, 2017), can be reduced by using a soothing technique. For example, a moving average method is used in this study. A cell-to-cell method proposed by Truong-Hong and Lindenbergh (2019) can be an alternative method applied for a structural surface. Irrespective of smoothing techniques applied, the spatial interval (or a spacing interval) should be used rather than the number of points because of the uneven distribution of the point clouds. Moreover, the use of the spatial interval can cause discontinuity deformation between adjacent intervals, which can be solved by using multiple spatial intervals (Park *et al.*, 2017).

One of the advantages of structural assessment-based TLS data is that status of an entire structure can report details. Results can be integrated into a BIM model allowing inspection, monitoring and assessment of an entire structure (Nguyen *et al.*, 2020). Moreover, as data acquisition and processing cost is significantly reduced, the structure can be monitored and inspected with higher frequency, and structural deficiencies can be detected earlier. However, the accuracy of the scanning TLS scan is often about 1–2 mm (Faro, 2020b, Leica Geosystems, 2021), which still exceeds an allowable error in measuring the deformation of a specific structure. Moreover, a high accuracy of resulting point clouds is achieved when an optimal sampling step is used. Lichti and Jamtsho (2006) concluded that the optimal sampling step is equal to 86% of the width of the laser beam, which was based on analysing 11 commercial TLS scanners with a scanning range of about 50 m. Soudarissanane *et al.* (2011) and Laefer *et al.* (2009) reported that the orthogonal distance from the scanner to a surface is dominating accuracy of the point cloud, while a scanning angle should be less than 60 degrees. The total error budget should be considered as a critical key factor in selecting TLS to estimate deformation of a structure

6. Conclusions
Laser scanning, particularly TLS, captures surfaces of structures with high accuracy and low cost in operation. However, in practice, using TLS for structural assessment through deformation measurement has many challenges, mainly relating to the point cloud registration error, surface extraction and selection of a reference surface, and available outlier, noisy data and/or mixed pixels. This study illustrates the use of TLS data in estimating deformations for various types of structures, including a masonry bridge

abutment, building slabs from a construction project and a steel girder supporting an oil tank roof. This work is to demonstrate a procedure to estimate deformation of the structure and explore the impact of these challenges on resulting deformation estimation of the structure.

The study shows that both RANSAC and region growing–based methods (CRG/VRG) can be extracted data points of surfaces, but RANSAC is only applicable for a primary primitive surface (e.g. a plane in this study) subjected to a small deformation (case study 2 and 3) and cannot eliminate mixed pixels. On the other hand, CRG and VRG impose a suitable method applied for deformed, free-form surfaces. Moreover, CRG and VRG are also better than RANSAC in eliminating mixed pixels and noisy data. That would consequently report reliable and accurate deformation of the structure.

In addition, in practice, a reference surface of a structure is mostly not available. The use of a fitting plane based on a point cloud of an existing surface would cause unrealistic and inaccurate deformation because outlier and data points of damaged areas affect an accuracy of the fitting plane. This study would recommend using the reference surface determined based on a design concept/specification. Finally, the quality of point clouds, which are mainly dominated by outlier, noisy data, mixed pixels and a registration error, is also a critical factor in obtaining reliable and accurate deformation. Smoothing methods can be reduced a negative impact on the data quality; however, a noise level of data and the registration error are still needed to minimize, and the mixed pixels must be priority filter out a data set before computing deformation.

References

American Petroleum Institute (2014), *API 650: Tank Inspection, Repair, Alteration, and Reconstruction*, API, Washington, DC.

Armesto-González, J., Riveiro-Rodríguez, B., González-Aguilera, D. and Rivas-Brea, M.T. (2010), "Terrestrial laser scanning intensity data applied to damage detection for historical buildings", *Journal of Archaeological Science*, Vol. 37, pp. 3037-3047, doi: 10.1016/j.jas.2010.06.031.

Bertacchini, E., Boni, E., Capra, A., Castagnetti, C. and Dubbini, M. (2010), *Terrestrial Laser Scanner for Surveying and Monitoring Middle Age Towers. XXIV FIG International Congress 2010-Facing the Challenges-Building the Capacity*, FIG Federation International des Geometres, Sydney, pp. 1-13.

Bhadrakom, B. and Chaiyasarn, K. (2016), "As-built 3D modeling based on structure from motion for deformation assessment of historical buildings", *International Journal of GEOMATE*, Vol. 11, pp. 2378-2384.

Boardman, C. and Bryan, P. (2018), *3D Laser Scanning for Heritage: Advice and Guidance on the Use of Laser Scanning in Archaeology and Architecture*, 3rd ed., English Heritage, Swindon.

Bosché, F. (2010), "Automated recognition of 3D CAD model objects in laser scans and calculation of as-built dimensions for dimensional compliance control in construction", *Advanced Engineering Informatics*, Vol. 24, pp. 107-118, doi: 10.1016/j.aei.2009.08.006.

Bosché, F. and Guenet, E. (2014), "Automating surface flatness control using terrestrial laser scanning and building information models", *Automation in Construction*, Vol. 44, pp. 212-226, doi: 10.1016/j.autcon.2014.03.028.

Boyko, A. and Funkhouser, T. (2011), "Extracting roads from dense point clouds in large scale urban environment", *ISPRS Journal of Photogrammetry and Remote Sensing*, Vol. 66, pp. S2-S12, doi: 10.1016/j.isprsjprs.2011.09.009.

Cabaleiro, M., Lindenbergh, R., Gard, W.F., Arias, P. and Van De Kuilen, J.W.G. (2017), "Algorithm for automatic detection and analysis of cracks in timber beams from LiDAR data", *Construction and Building Materials*, Vol. 130, pp. 41-53, doi: 10.1016/j.conbuildmat.2016.11.032.

Cabaleiro, M., Riveiro, B., Conde, B. and Sánchez-Rodríguez, A. (2020), "A case study of measurements of deformations due to different loads in pieces less than 1 m from lidar data", *Measurement*, Vol. 151, p. 107196, doi: 10.1016/j.measurement.2019.107196.

Cheng, L., Chen, S., Liu, X., Xu, H., Wu, Y., Li, M. and Chen, Y. (2018), "Registration of laser scanning point clouds: a review", *Sensors*, Vol. 18, doi: 10.3390/s18051641.

Cloudcompare (2021), "CloudCompare", 2.10 ed., available at: http://www.cloudcompare.org/.

Faro (2020a), *PointSense Basic and PointSense Pro*, Faro, available at: https://faro.app.box.com/s/x6yjjnzyi73fpk0y5ueeppfiw36d4hri/file/255567918254 (accessed 7 April 2021).

Faro (2020b), *Technical Specification Sheet for the Focus3D X 30/130/330 and X 130/330 HDR*, Faro, available at: https://knowledge.faro.com/Hardware/3D_Scanners/Focus/Technical_Specification_Sheet_for_the_Focus3D_X_30-130-330_and_X_130-330_HDR (accessed 7 April 2021).

Leica Geosystems (2020), "Leica Cyclone", available at: https://leica-geosystems.com/products/laser-scanners/software/leica-cyclone (accessed 15 December 2020).

Leica Geosystems (2021), *Leica ScanStation P20*, Leica Geosystems, available at: https://w3.leica-geosystems.com/downloads123/hds/hds/scanstation_p20/brochures-datasheet/leica_scanstation_p20_dat_en.pdf (accessed 2 June 2021).

Giardina, G., Milillo, P., Dejong, M.J., Perissin, D. and Milillo, G. (2019), "Evaluation of InSAR monitoring data for post-tunnelling settlement damage assessment", *Structural Control and Health Monitoring*, Vol. 26, p. e2285, doi: 10.1002/stc.2285.

Girardeau-Montaut, D., Roux, M., Marc, R. and Thibault, G. (2005), "Change detection on points cloud data acquired with a ground laser scanner", *International Archives of Photogrammetry, Remote Sensing and Spatial Information Sciences*, Vol. 36, p. W19.

Haddad, N.A. (2011), "From ground surveying to 3D laser scanner: a review of techniques used for spatial documentation of historic sites", *Journal of King Saud University - Engineering Sciences*, Vol. 23, pp. 109-118, doi: 10.1016/j.jksues.2011.03.001.

Harmening, C. and Neuner, H. (2020), "A spatio-temporal deformation model for laser scanning point clouds", *Journal of Geodesy*, Vol. 94, p. 26, doi: 10.1007/s00190-020-01352-0.

Hough, P.V., "Machine analysis of bubble chamber pictures", *Proc. of the International Conference on High Energy Accelerators and Instrumentation*, Sept. 1959, 1959, pp. 554-556.

Jafari, B., Khaloo, A. and Lattanzi, D. (2017), "Tracking structural deformations via automated sample-based point cloud analysis", *Computing in Civil Engineering*, Vol. 2017, pp. 403-410, doi: 10.1061/9780784480823.048.

Jiang, Q., Shi, Y.-E., Yan, F., Zheng, H., Kou, Y.-Y. and He, B.-G. (2021), "Reconstitution method for tunnel spatiotemporal deformation based on 3D laser scanning technology and corresponding instability warning", *Engineering Failure Analysis*, Vol. 125, p. 105391, doi: 10.1016/j.engfailanal.2021.105391.

Kassotakis, N., Sarhosis, V., Riveiro, B., Conde, B., D'altri, A.M., Mills, J., Milani, G., De Miranda, S. and Castellazzi, G. (2020), "Three-dimensional discrete element modelling of rubble masonry structures from dense point clouds", *Automation in Construction*, Vol. 119, p. 103365, doi: 10.1016/j.autcon.2020.103365.

Kavvadas, M.J. (2005), "Monitoring ground deformation in tunnelling: current practice in transportation tunnels", *Engineering Geology*, Vol. 79, pp. 93-113, doi: 10.1016/j.enggeo.2004.10.011.

Laefer, D.F. (2020), "Harnessing remote sensing for civil engineering: then, now, and tomorrow", in Ghosh, J.K. and Da Silva, I. (Eds), *Applications of Geomatics in Civil Engineering, 2020*, Springer, Singapore, pp. 3-30.

Laefer, D.F. and Pradhan, A.R. (2006), "Evacuation route selection based on tree-based hazards using LiDAR and GIS", *ASCE Journal of Transportation Engineering*, Vol. 132, pp. 312-320, doi: 10.1061/(ASCE)0733-947X(2006)132:4(312).

Laefer, D.F., Fitzgerald, M., Maloney, E.M., Coyne, D., Lennon, D. and Morrish, S.W. (2009), "Lateral image degradation in terrestrial laser scanning", *Structural Engineering International*, Vol. 19, pp. 184-189, doi: 10.2749/101686609788220196.

Laefer, D.F., Truong-Hong, L., Carr, H. and Singh, M. (2014), "Crack detection limits in unit based masonry with terrestrial laser scanning", *NDT and E International*, Vol. 62, pp. 66-76, doi: 10.1016/j.ndteint.2013.11.001.

Laefer, D.F. and Truong-Hong, L. (2017), "Toward automatic generation of 3D steel structures for building information modelling", *Automation in Construction*, Vol. 74, pp. 66-77, doi: 10.1016/j.autcon.2016.11.011.

Lague, D., Brodu, N. and Leroux, J. (2013), "Accurate 3D comparison of complex topography with terrestrial laser scanner: application to the Rangitikei canyon (NZ)", *ISPRS Journal of Photogrammetry and Remote Sensing*, Vol. 82, pp. 10-26, doi: 10.1016/j.isprsjprs.2013.04.009.

Li, D., Liu, J., Feng, L., Zhou, Y., Liu, P. and Chen, Y.F. (2020), "Terrestrial laser scanning assisted flatness quality assessment for two different types of concrete surfaces", *Measurement*, Vol. 154, p. 107436, doi: 10.1016/j.measurement.2019.107436.

Lichti, D.D. and Jamtsho, S. (2006), "Angular resolution of terrestrial laser scanners", *The Photogrammetric Record*, Vol. 21, pp. 141-160, doi: 10.1111/j.1477-9730.2006.00367.x.

Lichti Derek, D., Gordon Stuart, J. and Tipdecho, T. (2005), "Error models and propagation in directly georeferenced terrestrial laser scanner networks", *Journal of Surveying Engineering*, Vol. 131, pp. 135-142, doi: 10.1061/(ASCE)0733-9453(2005)131:4(135).

Lichti, D., Gordon, S., Stewart, M., Franke, J. and Tsakiri, M. (2002), "Comparison of digital photogrammetry and laser scanning", *Proc. International Society for Photogrammetr and Remote Sensing*, pp. 39-44.

Lindenbergh, R. and Pietrzyk, P. (2015), "Change detection and deformation analysis using static and mobile laser scanning", *Applied Geomatics*, Vol. 7, pp. 65-74, doi: 10.1007/s12518-014-0151-y.

Liu, W., Chen, S. and Hauser, E. (2011), "Lidar-Based bridge structure defect detection", *Experimental Techniques*, Vol. 35, pp. 27-34, doi: 10.1111/j.1747-1567.2010.00644.x.

Mizoguchi, T., Koda, Y., Iwaki, I., Wakabayashi, H., Kobayashi, Y., Shirai, K., Hara, Y. and Lee, H.-S. (2013), "Quantitative scaling evaluation of concrete structures based on terrestrial laser scanning", *Automation in Construction*, Vol. 35, pp. 263-274, doi: 10.1016/j.autcon.2013.05.022.

Montillet, J.-P., Szeliga Walter, M., Melbourne Timothy, I., Flake Rex, M. and Schrock, G. (2016), "Critical infrastructure monitoring with global navigation satellite systems", *Journal of Surveying Engineering*, Vol. 142, 04016014, doi: 10.1061/(ASCEU.1943-5428.0000181.

Mukupa, W., Roberts, G.W., Hancock, C.M. and Al-Manasir, K. (2017), "A review of the use of terrestrial laser scanning application for change detection and deformation monitoring of structures", *Survey Review*, Vol. 49, pp. 99-116, doi: 10.1080/00396265.2015.1133039.

Nguyen, T.A., Do, S.T., Hoang, H., Nguyen, K.D., Huynh, H.H., Che, D.H. and Nguyen, D.H. (2020), "Application of augmented reality for simulating 3D model from point cloud and photogrammetry – a study case of construction site inspection", *Vietnamese Journal of Construction*, Vol. 4, pp. 4-8.

Olsen Michael, J., Kuester, F., Chang Barbara, J. and Hutchinson Tara, C. (2010), "Terrestrial laser scanning-based structural damage assessment", *Journal of Computing in Civil Engineering*, Vol. 24, pp. 264-272, doi: 10.1061/(ASCEP.1943-5487.0000028.

Paffenholz, J., Vennegeerts, H. and Kutterer, H. (2008), "High frequency terrestrial laser scans for monitoring kinematic processes", *UNGEO 2008-4th International Conference on Engineering Surveying*, Bratislava, Slovakia, October 23-24, 2008, 13.

Park, S.W., Oh, B.K. and Park, H.S. (2017), "Terrestrial laser scanning-based stress estimation model using multi-dimensional double layer lattices", *Integrated Computer-Aided Engineering*, Vol. 24, pp. 367-383, doi: 10.3233/ICA-170548.

Pesci, A., Teza, G., Bonali, E., Casula, G. and Boschi, E. (2013), "A laser scanning-based method for fast estimation of seismic-induced building deformations", *ISPRS Journal of Photogrammetry and Remote Sensing*, Vol. 79, pp. 185-198, doi: 10.1016/j.isprsjprs.2013.02.021.

Rabbani, T., Heuvel, F.V.D. and Vosselmann, G. (2006), "Segmentation of point clouds using smoothness constraint", *International Archives of Photogrammetry, Remote Sensing and Spatial Information Sciences*, Vol. 36, pp. 248-253.

Riveiro, B., González-Jorge, H., Varela, M. and Dv, J. (2013), "Validation of terrestrial laser scanning and photogrammetry techniques for the measurement of vertical under clearance and beam geometry in structural inspection of bridges", *Measurement*, Vol. 46, pp. 784-794, doi: 10.1016/j.measurement.2012.09.018.

Rusu, R.B., Marton, Z.C., Blodow, N., Dolha, M. and Beetz, M. (2008), "Towards 3D Point cloud based object maps for household environments", *Robotics and Autonomous Systems*, Vol. 56, pp. 927-941, doi: 10.1016/j.robot.2008.08.005.

Schnabel, R., Wahl, R. and Klein, R. (2007), "Efficient RANSAC for point-cloud shape detection", *Computer Graphics Forum*, Vol. 26, pp. 214-226.

Sedek, M. and Serwa, A. (2016), "Development of new system for detection of bridges construction defects using terrestrial laser remote sensing technology", *The Egyptian Journal of Remote Sensing and Space Science*, Vol. 19, pp. 273-283, doi: 10.1016/j.ejrs.2015.12.005.

Son, H. and Kim, C. (2010), "3D structural component recognition and modeling method using color and 3D data for construction progress monitoring", *Automation in Construction*, Vol. 19, pp. 844-854, doi: 10.1016/j.autcon.2010.03.003.

Soudarissanane, S., Lindenbergh, R., Menenti, M. and Teunissen, P. (2011), "Scanning geometry: influencing factor on the quality of terrestrial laser scanning points", *ISPRS Journal of Photogrammetry and Remote Sensing*, Vol. 66, pp. 389-399, doi: 10.1016/j.isprsjprs.2011.01.005.

Suchocki, C. and Błaszczak-Bąk, W. (2019), "Down-sampling of point clouds for the technical diagnostics of buildings and structures", *Geosciences*, Vol. 9, doi: 10.3390/geosciences9020070.

Suchocki, C., Damięcka-Suchocka, M., Katzer, J., Janicka, J., Rapiński, J. and Stałowska, P. (2020), "Remote detection of moisture and bio-deterioration of building walls by time-of-flight and phase-shift terrestrial laser scanners", *Remote Sensing*, Vol. 12, doi: 10.3390/rs12111708.

Tan, K., Cheng, X., Ju, Q. and Wu, S. (2016), "Correction of mobile TLS intensity data for water leakage spots detection in metro tunnels", *IEEE Geoscience and Remote Sensing Letters*, Vol. 13, pp. 1711-1715, doi: 10.1109/LGRS.2016.2605158.

Tang, P., Huber, D. and Akinci, B. (2011), "Characterization of laser scanners and algorithms for detecting flatness defects on concrete surfaces", *Journal of Computing in Civil Engineering*, Vol. 25, pp. 31-42, doi: 10.1061/(ASCEP.1943-5487.0000073.

Teza, G., Galgaro, A. and Moro, F. (2009), "Contactless recognition of concrete surface damage from laser scanning and curvature computation", *NDT and E International*, Vol. 42, pp. 240-249, doi: 10.1016/j.ndteint.2008.10.009.

Trimble (2020a), *Trimble RealWorks v11.2*, Trimble, available at: https://geospatial.trimble.com/products-and-solutions/trimble-realworks (accessed 15 January 2020).

Trimble (2020b), *Trimble TX8 Laser Scanner*, Trimble, available at: https://geospatial.trimble.com/products-and-solutions/trimble-tx8 (accessed 15 January 2020).

Truong-Hong, L. and Laefer, D.F. (2014), "Application of terrestrial laser scanner in bridge inspection: review and an opportunity", *37th IABSE Symposium: Engineering for Progress, Nature and People*, International Association for Bridge and Structural Engineering (IABSE), Madrid, Spain, 3-5 September 2014.

Truong-Hong, L. and Laefer, D.F. (2015a), "Quantitative evaluation strategies for urban 3D model generation from remote sensing data", *Computers and Graphics*, Vol. 49, pp. 82-91, doi: 10.1016/j.cag.2015.03.001.

Truong-Hong, L. and Laefer, D.F. (2015b), "Documentation of bridges by terrestrial laser scanner", *IABSE Conference: Structural Engineering: Providing Solutions to Global Challenges*,

International Association for Bridge and Structural Engineering (IABSE), Geneva, Switzerland, 23 – 25 September, pp. 1384-1391.

Truong-Hong, L. and Lindenbergh, R. (2019), "Measuring deformation of bridge structures using laser scanning data", *4th Joint International Symposium on Deformation Monitoring (JISDM)*, Athens, Greece, 15-17 May, 7.

Truong-Hong, L. and Lindenbergh, R. (2020), "Inspecting structural components of a construction project using laser scanning", *EG-ICE2020*, 1-4 July 2020, Berlin, Universitatsverlag der TU Berlin, pp. 352-362.

Truong-Hong, L., Laefer, D.F., Hinks, T. and Carr, H. (2012), "Combining an angle criterion with voxelization and the flying voxel method in reconstructing building models from LiDAR data", *Computer-Aided Civil and Infrastructure Engineering*, Vol. 28, pp. 112-129, doi: 10.1111/j.1467-8667.2012.00761.x.

Truong-Hong, L., Falter, H., Lennon, D. and Laefer, D.F. (2016), *Framework for Bridge Inspection with Laser Scanning. EASEC-14 Structural Engineering and Construction*, Ho CHi Minh, Vietnam.

Truong-Hong, L., Laefer, D. and Lindenbergh, R. (2019), "Automatic detection of road edges from aerial laser scanning data", *International Archives of the Photogrammetry, Remote Sensing and Spatial Information Sciences*, Vol. 42.

Valença, J., Puente, I., Júlio, E., González-Jorge, H. and Arias-Sánchez, P. (2017), "Assessment of cracks on concrete bridges using image processing supported by laser scanning survey", *Construction and Building Materials*, Vol. 146, pp. 668-678, doi: 10.1016/j.conbuildmat.2017.04.096.

Van Gosliga, R., Lindenbergh, R. and Pfeifer, N. (2006), "Deformation analysis of a bored tunnel by means of terrestrial laser scanning", *Image Engineering and Vision Metrology*, 25-27 September 2006 Dresden 25-27, ISPRS, pp. 167-172.

Vo, A.-V., Truong-Hong, L., Laefer, D.F. and Bertolotto, M. (2015), "Octree-based region growing for point cloud segmentation", *ISPRS Journal of Photogrammetry and Remote Sensing*, Vol. 104, pp. 88-100, doi: 10.1016/j.isprsjprs.2015.01.011.

Wang, Q., Sohn, H. and Cheng, J.C.P. (2016), "Development of a mixed pixel filter for improved dimension estimation using AMCW laser scanner", *ISPRS Journal of Photogrammetry and Remote Sensing*, Vol. 119, pp. 246-258, doi: 10.1016/j.isprsjprs.2016.06.004.

Xi, R., He, Q. and Meng, X. (2021), "Bridge monitoring using multi-GNSS observations with high cutoff elevations: a case study", *Measurement*, Vol. 168, p. 108303, doi: 10.1016/j.measurement.2020.108303.

Xie, Y., Tian, J. and Zhu, X.X. (2020), "Linking points with labels in 3D: a review of point cloud semantic segmentation", *IEEE Geoscience and Remote Sensing Magazine*, Vol. 8, pp. 38-59, doi: 10.1109/MGRS.2019.2937630.

Yigit, C.O., Alcay, S. and Ceylan, A. (2016), "Displacement response of a concrete arch dam to seasonal temperature fluctuations and reservoir level rise during the first filling period: evidence from geodetic data", *Geomatics, Natural Hazards and Risk*, Vol. 7, pp. 1489-1505, doi: 10.1080/19475705.2015.1047902.

Zogg, H.-M. and Ingensand, H. (2008), *Terrestrial Laser Scanning for Deformation Monitoring - Load Tests on the Felsanau Viaduct*, ISPRS Congress, Beijing, pp. 555-562.

Corresponding author
Linh Truong-Hong can be contacted at: l.truong@tudelft.nl